REVIEW ARTICLE OPEN

Check for updates

Transparent neural implantable devices: a comprehensive review of challenges and progress

Young Uk Cho[1,3], Se Lin Lim[2,3], Jung-Hoon Hong[1,3] and Ki Jun Yu[1,2]✉

The key to designing an implantable device lies in condensing the synergistic effects of diagnostic and therapeutic methods in a single tool. In conjunction with the integration of electrophysiology and optical modalities, a transparent neural interface alleviates challenges of conventional metal-based microelectrodes. In this review, the multimodal sensing and stimulation functionalities of recent research are addressed. Next, issues that arise when combining functionalities of conventional metal-based, opaque electrode arrays together with optical modalities—(1) photoelectric artifacts, (2) optical image blocking, and (3) light transmission efficiency—are introduced. Then, an introduction of advancing material candidates for transparent neural interfaces follows with the latest research.

npj Flexible Electronics (2022)6:53 ; https://doi.org/10.1038/s41528-022-00178-4

INTRODUCTION

Flexible neural implantable systems that provide intimate and intuitive interfaces with a soft neural tissue serve as powerful tools for identifying complex neural circuits for diagnosing and treating neurological diseases[1–4]. Furthermore, recent efforts into simultaneously integrating multiple modalities with a single system for active recordings and actuations are of potential interest[5–8]. In particular, a hybrid of electrophysiological and optical approaches for neural implants maximizes the synergism of the resolution of the two methods, while at the same time compensating for the weaknesses of each approach[9–12]. However, in conventional device design, the two methods may conflict with each other in the process of data acquisition, such as electrophysiological readout, fluorescence cell imaging, or structural dynamics of the brain[3,13,14]. For example, when optical imaging, used to understand the structural and functional properties of the brain, is accompanied by opaque electrodes, there is great difficulty in analyzing the optical activation signals due to the visually obscured cells[15–17]. Even when applying optogenetics to treat neurodegenerative diseases, such as Parkinson's disease, epilepsy, or depression, is applied to an implantable device, serious electrophysiological signal contamination due to photoelectric artifacts occurs if optical transparency is not guaranteed[18–21]. Transparent implantable microelectrode arrays (MEAs) can simultaneously acquire high-resolution electrophysiological signals with negligible difference in performance from conventional electrodes while alleviating fundamental problems of optical modality[22–27]. Unlike metal based opaque MEAs, transparent electrodes eliminate the drawbacks of multimodal systems in that they can be used to measure electrical signals from the brain in real time without optical interference through material and structural controls. Transparent, implantable electrodes are fabricated with carbon-based materials[27,28], conductive polymers[29–31], and metal nanowires[32–34], which are primarily exploited in flexible electronics. In addition, transparent electrodes can be obtained by the geometrical design of materials for the electrodes. For instance, in the case of opaque metal, it is possible to obtain optical transparency by forming mesh-like or porous structures on the active materials, while also maintaining electrical properties like that of a conventional metal film[35–37]. Furthermore, to overcome the difficulty of securing both high electrical conductivity and optical transmittance, recent studies are focused on overcoming the disadvantages by mixing two or more materials[29,38,39]. Figure 1 shows the schematic overview of this paper. In this review, electrophysiological/optical diagnosis and treatment modalities are discussed, and the latest studies integrating these two approaches are introduced. Next, issues that arise when conventional opaque implantable electrode arrays are applied to optogenetics and optical imaging—photoelectric artifacts, optical image blocking, and less light transmission are the cases. Finally, a method for fabricating a transparent electrode that can solve these problems is presented by subdividing it into two categories: from a material point of view and from a structural point of view. As for the material approach of fabricating transparent neural electrodes, an introduction of intrinsically transparent material candidates, such as graphene, carbon nanotubes (CNT), conductive hydrogel, oxides, and conductive polymers, in addition to the latest research are discussed. Lastly, an introduction to research applied to biomedical engineering for a transparent electrode through a special structure is examined. This review consequently suggests the importance of transparent implantable devices for biomedical engineering and medical applications as a next-generation multimodal system for future research.

ELECTRICAL & OPTICAL MODALITIES

Recently, implantable neural devices that can identify complex neuronal circuits and diagnose and treat neurodegenerative diseases have been extensively studied[40–42]. Among them, the electrophysiological approach is a representative method for analyzing neuro-dynamics and neurological disorders[43,44]. The biggest advantage of an implantable device for electrophysiological recording is that it exhibits high temporal resolution as it can be exploited to measure biological signals in real time[45]. This property is advantageous for pathological diagnosis due to its potential for sophisticated analysis of signal transmission, even

[1]Department of Electrical and Electronic Engineering, Yonsei University, Seoul, Korea. [2]Department of Electrical and Electronic Engineering, YU-Korea Institute of Science and Technology Institute, Yonsei University, Seoul, Korea. [3]These authors contributed equally: Young Uk Cho, Se Lin Lim, Jung-Hoon Hong. ✉email: kijunyu@yonsei.ac.kr

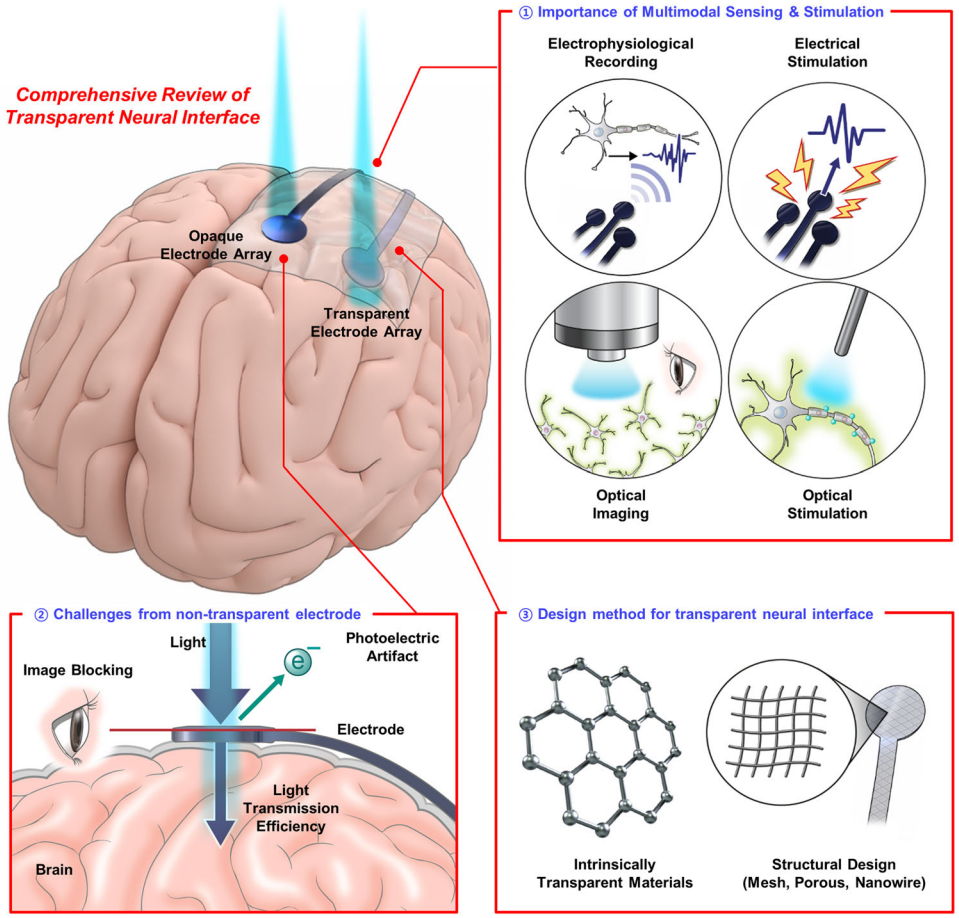

Fig. 1 A schematic introduction of the comprehensive review of the transparent neural interface. Schematic illustration of issues with transparent neural interface. (1) Importance of multimodal sensing & stimulation, (2) Challenges from non-transparent electrode, (3) Design method for transparent neural interface.

from a single neuron[46]. However, the methods of inserting devices into the brain or other organs are spatially limited because they can be operated only at the implant site. From an electrophysiological point of view, 'spatial resolution' varies greatly depending upon the size and spacing of electrodes for measuring neural activity. Especially, size of the electrophysiological sensing site is a significantly important factor in the performance and sensitivity of the neural interface. For example, although it has an advantage of being able to measure the activity of individual neurons in proximity with a small recording site (<1000 um^2), it is unavoidable from degradation of signal quality due to an increased electrochemical impedance. Therefore, for high spatial resolution electrophysiological recording, the size of the electrode densely distributed on a tissue should be reduced as much as possible to increase selectivity maintaining a low impedance value[41]. In other words, a device without empty measurement sites with dense electrodes in the same implanted area has high spatial resolution. In the case of a passive electrode array composed of one channel per one conductive interconnect, dense arrangement of recording channels is difficult due to wiring spatial charge for signal transmission. This is the reason that the spatial resolution of the electrophysiological approach is lower than that of the optical approaches[47]. To overcome this weakness, as shown in Fig. 2a, devices comprised of high-density, multi-channel electrode arrays are being thoroughly studied[48,49]. However, it is not entirely free from spatial constraints compared to optical approaches, such as magnetic resonance imaging (MRI), computed tomography (CT), or positron emission tomography (PET), which structurally analyze the brain or target organs.

In addition to the brain structure imaging approaches mentioned above, several optical approaches can observe brain activation on a cell-by-cell basis[50,51] (Fig. 2b). Optical imaging approaches are largely divided into methods of molecular selective neuro-dynamics identification using fluorescent[52–55] and voltage-sensitive dyes, and methods analyzing intrinsic scattering and oxygenated condensation changes in brain tissue such as optical coherence tomography (OCT)[56,57] and diffuse optical tomography (DOT)[58,59]. An advantage of using optical recording is that it shows a better spatial resolution compared to the electrophysiological approach because the desired site can be observed broadly without a spatial disruption of the implanted site. Voltage sensitive dye imaging is a method of measuring neural activity using molecules that can modify electric charges from neural circuits into fluorescence of emitted light. Since this method provides only the surface activity of the brain in nearly two dimensions, it is difficult to see the activity of the deep brain relative to the electrophysiology through the penetrating probe[60–62]. However, this approach is particularly important when neural activities occur in many cells or multiple sites simultaneously, such as in the nerves or brain. It is also advantageous when observing cells that are too narrow for electrophysiological recording or cells prone to damage. Particularly, calcium transient fluorescence of neurons or HbT imaging, which is a method measuring changes in oxygen saturation of hemoglobin, are representative methods to study

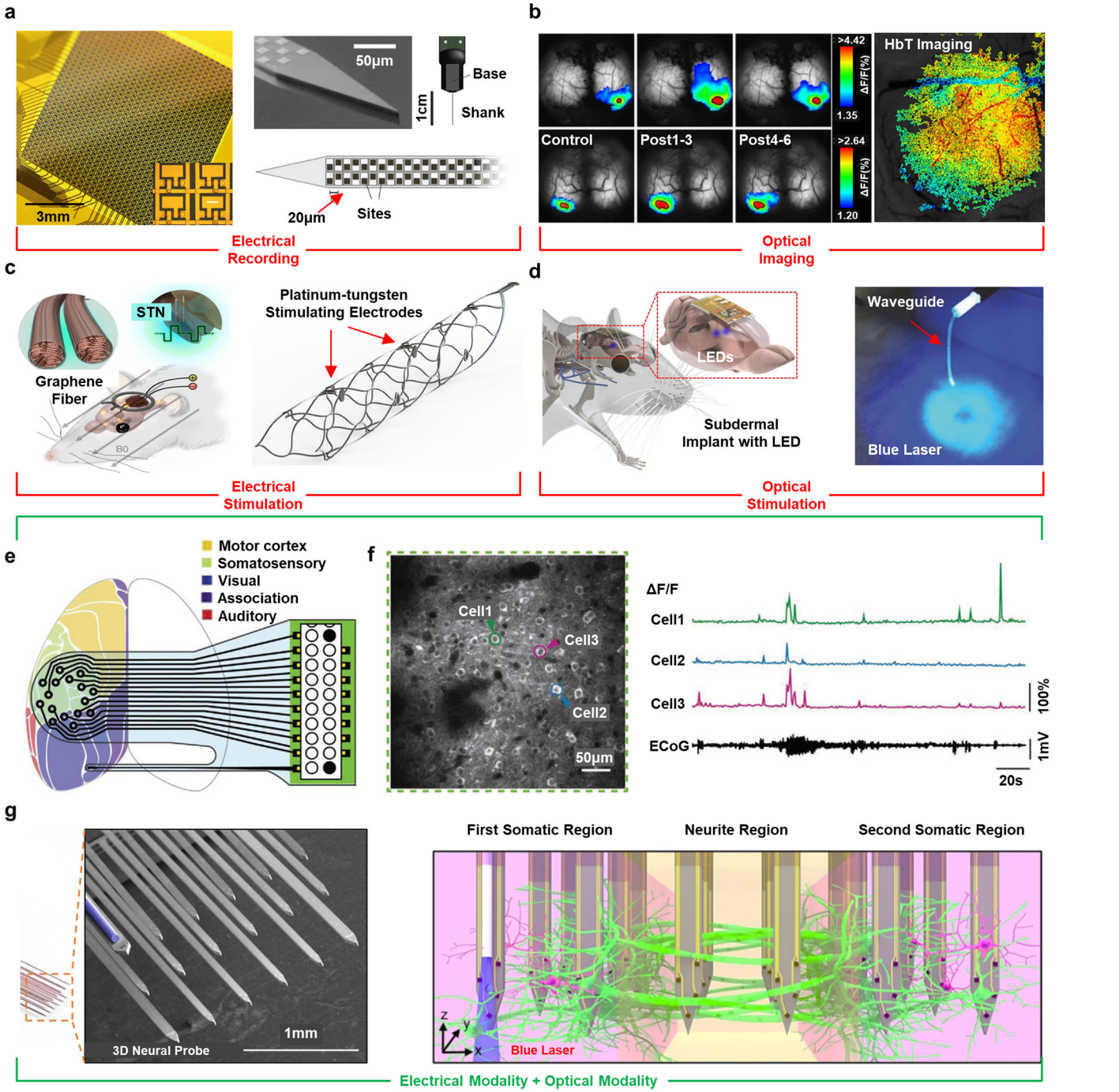

Fig. 2 Integration with electrophysiology and optical modalities by neural implantable device. a High-density active electrode array for electrophysiological brain mapping (left) and a high-density, active-matrix neural probe for deep brain recording (right). **b** Transcranial Ca^{2+} transient imaging from a visual flash response of anesthetized mouse (left) and total hemoglobin imaging of a mouse cortex after hind-paw stimulation (right). **c** Graphene fiber-based neural electrode for electrical stimulation of subthalamic nucleus (left) and endovascular stent for focal electrical stimulation of the sheep motor cortex (right). **d** Soft, fully implantable optoelectronic system for light stimulation of nucleus accumbens (left) and ultrasoft-hydrogel optical fibers for optogenetics stimulation (right). **e** Stretchable electrocorticography (ECoG) array for simultaneous electrophysiological recording with optogenetics stimulation. **f** Two-photon fluorescence imaging of GcaMP6f-labeled neurons from a SNAP25-GCaMP6f mouse (left) and corresponding calcium transient from each cell in colored circles from imaging and ECoG signals from the electrode (right). **g** Three-dimensional multi-shank probe for simultaneous electrical modality, optical modality, and drug delivery. A magnified image of the device is presented with an optical waveguide (left). The connectivity from a first somatic region to a second somatic region is illustrated with a three-dimensional structure of the multi-shank probe (right). Panel a reprinted with permissions from ref. [48,49], AAAS (left) and Springer Nature (right). Panel b reprinted with permissions from ref. [50,51], Springer Nature (left) and Elsevier (right). Panel c reprinted with permissions from ref. [77,78], Springer Nature. Panel **d** reprinted with permissions from ref. [81,82], Springer Nature (left) and Wiley (right). Panel e and f reprinted with permissions from ref. [85], Wiley. Panel g reprinted with permissions from ref. [86], Springer Nature.

the spatial activity of neuronal populations[63–65]. These approaches show excellent temporal resolution of up to 3–10 ms depending on the tissue staining method or the resolution of microscopy, but they require integration with near-real-time electrophysiological recording methods (~1 ms) to function as clinical applications[17,66].

The method of 'treatment' beyond the simple 'diagnosis' of neural activity is also important in terms of the functionalities of implantable devices. There are several ways to modulate brain nerve activity, including electrical stimulation[67,68], light stimulation[69–71], drug delivery[72–74], and magnetic stimulation[75,76]. Among the electrophysiological treatments, the most representative approach is electrical stimulation, which is the process of modulating the neuronal activity and firing patterns through current or voltage by inserting an electrically conducting microelectrode into the body[77,78] (Fig. 2c). Electrical stimulation has been already widely used clinically for decades as its therapeutic effect is guaranteed. However, this is limited as local stimulation to a specific area is impossible due to the undesired excitation of neighboring neurons[79,80]. To overcome this issue, optogenetic stimulation that can precisely control the neural activity of target neurons through light has been rigorously studied[81,82] (Fig. 2d). Optical stimulation exhibits excellent selectivity to neurons because it changes neuro-dynamics by attaching light-sensitive proteins, such as channel rhodopsin (ChR2) or halo rhodopsin (HR), and then applies a specific wavelength of light. This method allows versatile, cell type-specific light-based control of cellular activity in diverse set of cells, circuits and brain structures than that of an electrical stimulation.

A multimodal implantable device is a neuro-prosthetic that can be applied as a single tool that integrates various methods of both recording the above-mentioned neural activity and treating diseases. Neural electrode array for electrophysiology is largely divided depending on the site of implantation in the brain-electrocorticography (ECoG) and penetrating probe. In particular, ECoG has an advantage of capturing neural activities of epilepsy or neuro-degenerative disorder more broadly than that of penetrating probe. Since the ECoG is a method of measuring the integrated activity (field potentials) of thousands to millions of nerve cells, the signals from the ECoG has become an important clue pathological diagnosis[83,84]. The hybrid system of the electrophysiological and optical approaches maximizes the advantages of each method and complements the disadvantages of each method. Figure 2e shows the device configuration of a study in which two-photon calcium imaging and electrocorticography were simultaneously performed[85]. Fluorescence imaging of a large field of view helped analyze the neuronal activity more intuitively with an electrical signal recorded from the limited measurement of the electrodes (Fig. 2f). However, shadows from the recording electrode in the optical image imply that it was not completely free from optical blocking by the non-transparent electrode array. Additionally, the lack of a temporal sampling rate and the inaccuracy of fluorescence changes, which are main problems of the imaging methods, can be solved by ECoG recordings. Similarly, several attempts have been made to design a device that can bridge the gap between optogenetic and electrophysiological recordings. For example, there is a multi-shank probe that can be used to diagnose neural propagations transmitted through light stimulation by electrophysiological action potential analysis[86] (Fig. 2g). This 3D neural interface confirmed the functional connectivity of the two somatic regions through synaptic latency and transmission velocity while simultaneously analyzing the neural network by optical stimulation.

CHALLENGES FROM OPAQUE ELECTRODES

The most important part of combining electrophysiology and optical modality is that the data from the two methodologies should not be polluted the other and should generate diagnostic or therapeutic synergies with their own device characteristics. Recent studies have revealed that opaque electrodes based on conventional metals, such as gold or platinum, present new challenges and boundaries in the integration of electrophysiological and optical modalities. In this section, we discuss various problems that arise from multimodal diagnosis and treatment using opaque neural interfaces: photoelectric artifacts, optical image blocking, and light transmittance efficiency. Additionally, we also present how transparent devices can alleviate these problems. A summary of each issue is shown in Fig. 3a.

Photoelectric artifacts

In the field of neuroscience, the photoelectric effect generally refers to a phenomenon in which a potential difference occurs in an electrode when a metal electrode receives light and current flows at the surface of the electrode[18,19]. When diagnosing neuro-dynamics optically, such as fluorescence calcium imaging, the surrounding residual current does not have a significant effect on the cell. However, when the electrophysiological signal by optogenetics is recorded, the current around the electrode surface caused by light energy is the main source of data contamination and distortion. A photoelectric artifact in a metal-based microelectrode occurs only if it exceeds a specific minimum photon energy, termed the threshold wavelength, which can emit photoelectrons. Thus, threshold frequencies or photons have enough energy to emit electrons, depending on the proper material choice for the device. Figure 3b is a schematic diagram of the orbital energy level of an electron. This schematic suggests that the orbitals of all solid materials have bands of specific energy ranges. For example, the conduction band refers to the state in which electrons can escape from their atoms or molecules in the form of a free charge, and the valence band describes the region in which electrons are in the lowest energy state. In the case of metals, since the valence and conduction bands overlap with one another, there is almost no bandgap, so electrons are relatively easy to change into free charges. Since the semiconductor material has a small band gap, electrons can be delocalized into a conduction band by applying a certain amount of heat or light energy. In the case of an insulator, electrons cannot easily reach the conduction band by a small amount of heat or light energy, as it has a very large bandgap. The metal-based microelectrode has a high probability of causing photoelectric artifacts because the photo excitation of metal electrons is significantly easier than those of other materials[87,88]. Figure 3c shows electrophysiological signals contaminated by photoelectric artifacts. Photoelectric artifacts caused by laser pulse stimulation show similar tendencies to single-unit action potential waveforms. In the case where the amplitude of the voltage significantly increases at the start of light irradiation, it is easy to recognize that it is an onset noise caused by the light source. It is possible to minimize this problem through signal wave filtering or linear regression of the trace of the signal, as presented in Fig. 3d. However, for the signal that follows, it is unclear whether it is noise caused by photoelectric artifacts or a biological signal from an experimental model, so it has a great influence on the interpretation of electrophysiological results. To overcome this issue, optical stimulation of the brain was dominated by low-frequency or long rise time waves to reduce light-induced artifacts. These limitations frustrate the possibility of treating neurological diseases that require high-frequency light stimulation. In conclusion, to enable light stimulation in a wide frequency band without interference by artifacts, it is necessary to select an electrode material that hardly generates a photoelectric effect or to design a device with a special structure[89].

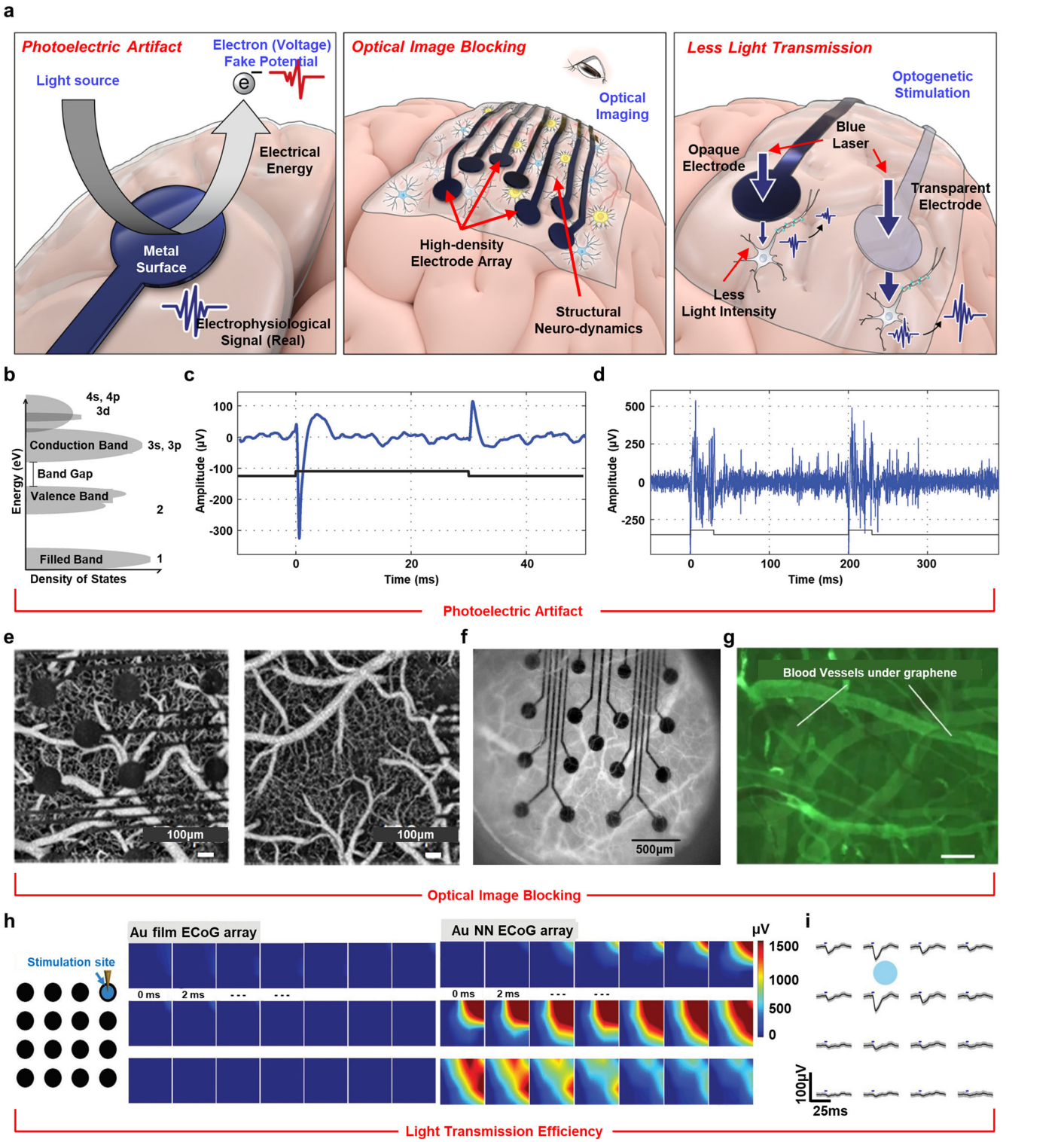

Fig. 3 Challenges with the integration of electrophysiological and optical modalities by non-transparent neural interfaces. a Schematic illustration of challenges from non-transparent electrode array with integration of optical modalities. **b** Orbital electron energy levels versus the density of each state. **c** Photoelectric artifact from electrophysiological signals from the brain after 473 nm photo-stimulation with an optical fiber. **d** The trace of electrophysiological signals from panel c. The photoelectric artifact is presented as the onset of stimulation. **e** Optical Coherence Tomography (OCT) imaging of a brain with a non-transparent platinum electrode array (left) and a transparent graphene electrode array (right). **f** An image of blood vessels from the brain cortex labeled with rhodamine-B dextran through the platinum electrode array from the cranial window. **g** Fluorescence image of blood vessels with a transparent graphene electrode array. **h** Spatiotemporal electrophysiological heatmap of a corresponding electrode channel upon illumination of the 473 nm laser directly on the surface of the Au film electrode (left), and an Au nanonetwork electrode (right). **i** Spatially distributed electrophysiological potentials from the optogenetic stimulation. The blue color represents the illumination spot. Panels b, c, and d reprinted with permissions from ref. [19], Royal Society of Chemistry. Panels e and g reprinted with permissions from ref. [16], Springer Nature. Panels f and i reprinted with permissions from ref. [90], IOP publishing. Panel h reprinted with permissions from ref. [18], Wiley.

Optical image blocking

Another issue that occurs when opaque electrodes are used for neural interfaces is tissue imaging occlusion by the electrodes. Brain imaging is a method of observing activated tissue with a high spatial resolution, without damaging cells by using a specific band of light. Beyond structural imaging of the brain, the biggest drawback of this functional imaging is that obtaining neurodynamic information with a high temporal resolution is difficult. To overcome this challenge, an integration of electrophysiological approaches that ensure real-time biological information is significantly important. Figure 3e shows an OCT image of a metal-based opaque electrode (left) and an OCT image of a transparent electrode (right)[16]. To analyze the electrophysiological signals from the brain, the implantable device is contacted on the surface of the tissue, and the opaque electrode directly covers the blood vessel and brain tissue to be observed. This problem not only impedes the interpretation of signal propagation in functionalized tissues, such as with voltage-sensitive dyes, but also makes it difficult to observe vascular changes and the dynamic activity of nerves. The weaknesses of using an opaque neural interface are deteriorated as the electrode channel density increases. In a passive device consisting of only conductive connections, the number of channels for recording electrodes and the size of the electrodes are severely limited because the number of connections required per electrode increases proportionally, as shown in Fig. 3f[90]. Conversely, in the case of a device in which all connections, including electrodes, are transparent, cell-specific activity can be confirmed without optical hindrance (Fig. 3g)[28].

Less light transmission

Brain stimulation through optical modality is affected by frequency and light intensity[91–93]. Therefore, it is evident that the neural interface, which is an intermediate pathway from the light to brain tissue, should not interfere with the light to reach the nervous tissue without significant energy loss. Figure 3h shows the light transmission efficiency of a transparent electrode by representing the optical stimulation from electrophysiological distribution using a pristine gold film electrode and a gold nanonetwork[18]. Optogenetic stimulation was performed directly above the surface of the electrodes, and, as the light intensity is the same, this suggests that the transparency of the electrode array critically affects light transmission. Schematics of brain color-mapping of light stimulation on the electrocorticography (ECoG) microelectrode array from gold film shows the electrode array absorbs most of the light, clearly demonstrating the failure of stimulation on a transgenic mice. Conversely, a gold nano-network electrode array showed the propagation of a relatively high amplitude potential from the same stimulation site to the surrounding area, proposing the possibility of significantly increasing the light transmission efficiency with the same material. Alternatively, as shown in Fig. 3i, the stimulation site can be set between the electrode arrays upon light illumination[90]. However, the expected electrophysiological signal cannot be obtained from the target neuron of the light stimulus when the position of the neuron is located just underneath the opaque electrode as it completely blocks the stimulus. The most ideal approach to overcome the aforementioned problems is to design electrodes through the engineering of materials and structures, thereby establishing user transparency of the materials. In the next section, we discuss the fabrication method of transparent electrodes by material and structure and its latest research.

TRANSPARENT IMPLANTS-FROM MATERIALS

This section discusses the fabrication of electrodes for neural interfaces using intrinsically transparent materials. Two representative methods of transparent neural interface fabrication utilize (1) intrinsic transparent materials and (2) structural modification of opaque materials. A detailed introduction of transparent material candidates is presented in Table 1. Transparent neural interfaces must ensure transparency to minimize light-induced artifacts, as well as conductivity to measure electrical signals[3,94]. To transmit neural signals properly, excellent electrochemical impedance between the electrode sensing site and tissue is also important. Moreover, the trace resistance between the sensing site and the percutaneous connecter becomes a dominant factor in obtaining high-quality electrophysiological signals. Assuming the same electrode interconnect line width and length, carbon or polymer-based electrodes have much more unfavorable electrical properties than metal wiring in terms of trace resistance. Therefore, in the case of a carbon-based neural electrode array, the interconnect line is mainly substituted with a conductive metal to make the electron path more intuitive, while giving up interconnect transparency. For polymer electrode arrays, the trace resistance is significantly reduced by changing the molecular structure through special doping or post treatment, maintaining the transparency of the entire device including conducting path[41,95]. Therefore, high transparency and conductivity should be the priority consideration when selecting materials for the design of multimodal devices. Recently, graphene has attracted much attention due to its advantageous properties associated with neural interfaces. Beyond its superior electrical conductivity, it also has excellent transparency due to its two-dimensional honeycomb structure. Moreover, its well-known mechanical characteristics, such as high tensile strength and high flexibility, also make graphene a promising material for reliable and robust flexible electronics. In this section, detailed properties and related studies on graphene are presented. Moreover, carbon nanotubes, which are rolled-up graphene sheets, conductive hydrogels with tissue-like Young's modulus, and transparent conducting oxides with low resistivity are also discussed.

Transparent graphene neural interface

Graphene, one of the most promising candidates for transparent neural interface fabrication, is a carbon-based 2D material arranged with a honeycomb-lattice structure[3,96,97]. Carbon-based materials are basically black soots which represents low light transmittance in bulk state. However, owing to negligible thickness of 2D monolayer graphene, which is much smaller than wavelength of the visible light, ideal 2D monolayer graphene shows tremendous visible light transmittance over 97%.[98,99]. Moreover, graphene has a superior intrinsic optical transparency of over 90% that covers ultraviolet (UV) and infrared (IR) light[16,100]. High visible light transmittance, which greatly reduces optical blocking, is critically important in transparent neural interfaces. Furthermore, high optical transmittance of the neural interface materials for both UV and IR light is highly advantageous in terms of optogenetic stimulation and photo-induced imaging[98]. Above all its great optical properties, this 2D monolayer material performs outstanding mechanical and chemical stability because of strong sp^2 bonding between carbon atoms[96,97,101]. For example, it has durable physical properties, such as a breaking strength of 42 N m^{-1} and a Young's modulus of 1.0 TPa[102]. In addition, as it features high electrical mobility, graphene is excellent material for flexible or stretchable electronics[103–107]. In this respect, recently, graphene-based flexible electrodes have been widely utilized as bio-integrated transparent electronics.

Most recent studies using intrinsically transparent materials utilize graphene as transparent electrodes owing to its outstanding electrical, mechanical, and optical properties[10,15,24,28,108,109]. Although graphene is not completely free from photoelectric artifacts, it shows powerful performance for an optical approach than metal electrodes with the low probability of photon energy excitation[28,110]. By using its broad wavelength

Table 1. Summary of material candidates for transparent neural interface.

Material	Composition (Electrode/ Substrate)	Electrode Fabrication Method	Electrical Property (Electrode Area)	Transmittance	Biocompatibility	Optical Property Demonstration	Ref.
Graphene	Nitric acid doped Graphene/Polyimide	Transfer Printing	541 kohm @ 1 kHz (50 μm × 50 μm)	Transparent above 450 nm	○	Calcium Imaging	24
	4-layered graphene/ Parylene C	Transfer Printing	(243.5 ± 5.9) kohm @1 kHz (~45240 μm^2)	>90% (470 nm, 570 nm)	○	Fluorescence & OCT imaging Optogenetics	28
	4-layered graphene/ Parylene C	Transfer Printing	(248.7 ± 125.0) kohm @1 kHz (17,671 μm^2)	N/A	N/A	Fluorescence Imaging	15
	4-layer graphene/PET	Transfer Printing	963 kohm @ 1 kHz (100 μm × 100 μm)	N/A	N/A	Deep two photon calcium Imaging Optogenetics	109
CNT	SWCNT/PDMS	Floating catalysis CVD	0.20 ± 0.03 Mohm @1 kHz (100 μm × 100 μm)	70–90% (550 nm)	N/A	Two photon Imaging Optogenetics	27
Hydrogel	PVA hydrogel/PDMS	Freeze-thaw	490 kohm @ 1 kHz (r = 1.5 mm, salt bridge width = 500 um)	50–60% (400–800 nm)	○	N/A	129
Conductive Oxides	ZnO&ITO/Parylene C	Mechanical Dicing/Chemical Etching	~400 kohm @ 1 kHz/ZnO ~0.15 ohm cm^{-1}/ITO 1.5 kohm cm^{-1}	>70% (visible light)	○	Optogenetics	144
PEDOT:PSS	PEDOT:PSS-EG/PET	Lift-off Spin coating	50–70 kohm @ 1 kHz (300 μm × 300 μm)	85% (400–700 nm)	◎	Optogenetics	154
	Graphene& PEDOT:PSS/ Glass	CVD Electroplating	166 ± 13 kohm @ 1 kHz (r = 15 μm)	84% (400–700 nm)	N/A	Fluorescence Imaging	152
Ag	Ag&Au Core Shell/ Parylene C	Spray coating Cyan-free Electroless Plating Pin-transfer	1.1–3.2 ohm cm^{-2} 15 ohm sq^{-1} (r = 130 μm)	69–83% (400–700 nm)	◎	Optogenetics	22
	AgNW&IZO/ Parylene C	Spray coating	6 ohm sq^{-1}/20 kohm @ 1 kHz (r = 250 μm)	>60% (550 nm)	N/A	Fluorescence Imaging	179
Au	Au nanonetwork	Nanopattern Electrospinning	11.8 k-33.9 kohm @ 1 kHz (r = 100 um)	75–81% (300–1200 nm)	◎	Optogenetics	171
	Au mesh with PEDOT: PSS/ Parylene dix-SR	Lift-off	10 kohm @ 1 kHz (PEDOT:PSS 1400 μm^2)	60% (475nm)	N/A	Optogenetics	167
	Au/PEDOT:PSS bilayer/ Parylene C	Lift-off Electroplating	130 kohm @ 1 kHz (314 μm^2)	70% (550 nm)	◎	Two photon Imaging	25
	Au honeycomb grid/ Parylene	Lift-off	8.14 ohm cm^2 /156.6 kohm @ 1 kHz (80 μm × 80 μm)	70% (550 nm)	◎	N/A	161
	Au grid/ ITO bilayer/PET	Lift-off	5.6 ± 0.7 ohm sq^{-1} /5.3 k @1 kHz (320 μm × 320 μm)	59–81% (550 nm)	◎	Optogenetics	162
	Au grid/ ITO island/PET	Lift-off	6.9 ± 0.6 ohm sq^{-1}/20.3 k @ 1 kHz (320 μm × 320 μm)	N/A	◎	Optogenetics	

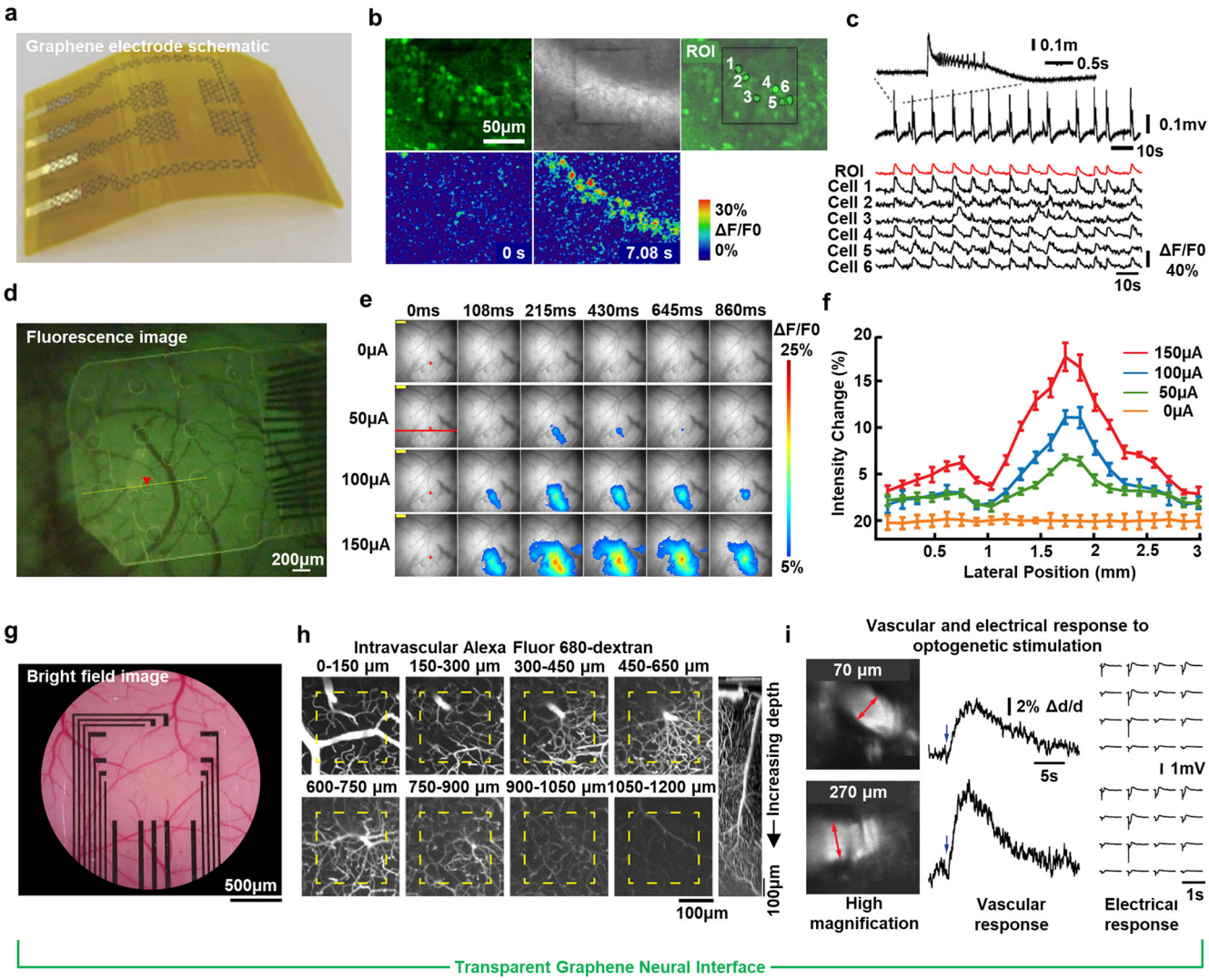

Fig. 4 Graphene-based transparent electrode array for simultaneous electrical and optical modalities. a Schematic of a graphene-based transparent neural interface. The honeycomb-lattice structure of graphene maximizes electrode transparency. **b** Calcium transient images under a graphene-based transparent electrode with 488 nm excitation wavelength. Six cells are numbered in the region of interest. Scale bar: 50 μm. **c** Correlation between electrophysiological signals reflecting manually induced interictal-like effects (top) and simultaneous ΔF/F0 curves for numbered cells in panel b (bottom). All data from panels b and c are observed simultaneously. **d** Fluorescence image of a GCaMP6f mice cortex under a transparent graphene electrocorticography (ECoG) array. Scale bar: 200 μm. **e** Spatiotemporal fluorescence recordings with various electrical stimulation amplitudes. **f** Plot of intensity changes versus the lateral position. The greatest intensity changes were detected at the stimuli point (between 1.5 and 2 mm). The lateral position axis corresponds to the horizontal red line in panel **e**. **g** Bright optical image of the transparent graphene electrode array on the brain surface. Scale bar: 500 μm. **h** Two-photon imaging at a depth of 1,200 μm under photoelectric artifact minimized graphene electrode. Scale bar: 100 μm. **i** Crosstalk-free detection of two-photon imaging and electrophysiological recording, according to simultaneous optogenetic stimulation. Panel a, b, and c adapted from ref. [24], Springer Nature Limited. Panel d, e, and f adapted with permission from ref. [15], American Chemical Society. Panel g, h, and i adapted from ref. [109], Springer Nature Limited.

transparency, a similarity between calcium imaging and electrophysiological signals was verified. Figure 4a shows a schematic illustration of a transparent neural interface using graphene. The transparency of the electrode is owing to the honeycomb-lattice structure of graphene as we can see in the figure[24]. Figure 4b illustrates fluorescent calcium images under the graphene electrode on a P12 mouse hippocampal slice using a 488 nm excitation wavelength. Modification of ion concentrations, such as potassium and magnesium ions, and bicuculline-methiodide were utilized to make spiking activities of the sample. Simultaneously, electrophysiological signals were recorded by the electrodes without noticeable laser-induced artifacts, and it is shown together, as illustrated in Fig. 4c, with calcium transients of the numbered cell. This implies that a strong correlation exists between fluorescence transients and electrophysiological signals using transparent graphene electrodes.

In general, graphene-based transparent neural interfaces requires a high quality graphene but the transfer process of the graphene on a subtrate make the fabrication complexity. In addition, light absorption and dissipation by the substrate site are critical in optical modalities. To maximize transparency of the electrode, a Parylene C and graphene-based transparent electrode was fabricated. A fluorescence image using the device is shown in Fig. 4d[15]. Charge density limitation for the four-layer graphene electrode was characterized based on EIS, CV, and a failure bench-testing method. Spatiotemporal responses with varying stimulation currents in the calculated range (approximately 150 μA) verified the correlation between the stimulation current and

neural activation represented as a fluorescence transient, as shown in Fig. 4e. Also, spatial response analysis proved that maximum activations of cells occur at the center of the stimuli (between 1.5 mm to 2 mm) as shown in Fig. 4f.

The capability of minimizing light-induced artifacts is a key feature of transparent neural interface. Although high-quality graphene produces negligible artifacts, ordinary graphene electrodes bring out unexpected artifacts due to defects or residues from the fabrication process. In this regard, graphene transparent electrodes with highly minimized artifacts were formed by improving the fabrication process. Figure 4g shows a bright field image of a 16-channel electrode device without any visible

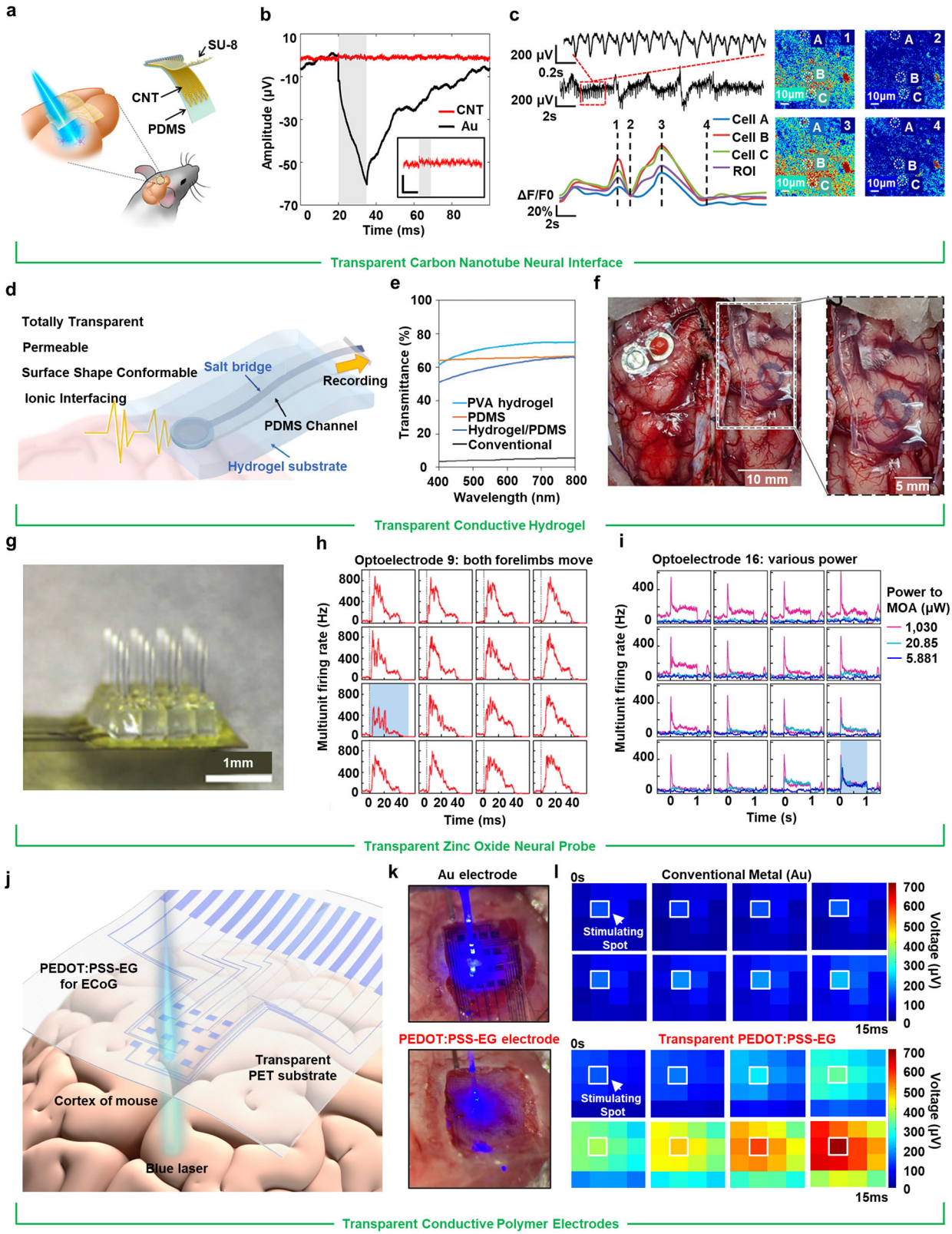

Fig. 5 Additional transparent materials for simultaneous electrical and optical modalities. a Carbon nanotube (CNT) transparent electrode array on a stretchable substrate. **b** Minimized light-induced artifact of a CNT electrode compared with a gold electrode. **c** Simultaneous electrode recording (top) and calcium transients under the CNT electrode (bottom) during seizure-like events. Two-photon images for dashed timelines on calcium transients (right). Scale bar: 10 µm (right). **d** Schematic illustration with highlighted features of a hydrogel-based transparent electrode. **e** Transmittance versus wavelength plot for hydrogel-based electrode materials. **f** Hydrogel-based and conventional electrode on the complicated surface of porcine brain. The hydrogel electrode performs better in terms of transparency and conformality to the surface. Scale bar: 10 mm (left), 5 mm (right). **g** 4 × 4 Zinc-Oxide-based (ZnO) transparent micro-opto-electrode array (MOA). Optogenetic stimuli was transmitted through the ZnO electrodes and emitted from the tip as waveguides. These pinpointed stimulations minimize spatial mismatches between the electrical and optical modalities. Scale bar: 1 mm. **h** High-powered optical stimulation to the motor cortex prompted various body movements. In the case of optoelectrode 9, both forelimbs reacted and corresponding electrical recordings are plotted. **i** Electrical recordings from an MOA when various powered optical stimulations were given to optoelectrode 16. **j** Transparent PEDOT:PSS-EG neural electrode array for simultaneous electrophysiology with optogenetics. **k** 473 nm light stimulation upon the electrode of Au array (Top) and PEDOT:PSS-EG array (Bottom), respectively. **l** Electrophysiological color-heatmap from light evoked signal response with conventional Au electrode array (Top) and transparent PEDOT:PSS-EG electrode array (Bottom). Panel a, b, and c adapted with permission from ref. [27], American Chemical Society. Panel d, e, and f adapted with permission from ref. [129], Springer Nature. Panel g, h, and **i** reprinted from ref. [144], Springer Nature. Panel j, k, and l adapted with permission from ref. [154], Springer Nature.

electrode sites[109]. In addition to the visible light transmittance, highly minimized artifacts allow deep two-photon imaging below the cortical surface under transparent electrodes[10]. Nevertheless, a two-photon excitation laser induces unnecessary artifacts which impede clear imaging, and the 1200 µm deep imaging of tissue beneath the electrode was successfully obtained as shown in Fig. 4h. Also, two-photon imaging, optogenetic stimulation, and large-scale hemodynamic response imaging were combined with electrophysiological recordings of the cortical surface without any noticeable interruptions. By using these crosstalk-free electrodes, simultaneous electrophysiological recording, and two-photon imaging of the cortical surface during optogenetic stimulation was achieved, as shown in Fig. 4i.

Other promising transparent implants

Transparent neural interfaces using intrinsically transparent materials other than graphene are also being widely investigated. Carbon nanotubes (CNTs), another highly conductive carbon-based material, is one of the more powerful candidates. A single CNT is rolled-up graphene sheet into a tube shape and is categorized as single-walled CNT (SWCNT) and multi-walled CNT (MWCNT), based on the number of graphene sheets[104,111,112]. A single CNT could have metallic or semiconductor properties depending on its chiral vector. In general, CNTs are a mixture of both metallic and semi-conducting CNTs, and their ideal separation is almost impossible due to van der Waals force attractions[113,114]. Therefore, the properties of CNTs are determined by adjusting their ratios. CNT electrodes maintain their conductivity through nanowire percolations. These nano mesh-like void networks and the electrode thickness far under visible light wavelength enable high light transmittance of CNT electrodes[99,115]. Even though CNTs are widely used to make transparent electrodes, optical incident orientation should be examined because of CNTs optical anisotropy. It is because of 1D structure and nanometer-scale diameter of CNT, which makes different optical strengths between tangential and parallel direction transitions based on its axes. In general, transmittance of CNTs electrode decreases as incident angle increases, so such optical property should be carefully considered[116,117]. Interestingly, in the CNT networks, the conductivity is limited by the outmost shell, even if the number of graphene sheets increases. Therefore, as the number of shells increases, a greater amount of light is absorbed, resulting in less light transmittance when the same conductivity is desired. As such, SWCNTs-based electrodes perform greater optical properties compared to MWCNTs electrodes in the same fabrication conditions[99]. In addition, its massive electrical conductivity and mobility make CNTs a highly applicable material for transparent neural interfaces[97,107,118]. Since CNTs can be dispersed into a variety of aqueous solutions, roll-to-roll fabrication, which has great a merit in industrial manufacturing, is possible[119].

In addition, the possibility of easy fabrication processes, such as solution-based spray coating, is a strong advantage compared to a method of forming transfer-based graphene electrodes[120,121]. A recent study shows highly stretchable transparent neural interfaces by patterning CNT film on an elastomer. Figure 5a displays a schematic illustration of the device and its functionality[27]. Carbon nanotube percolations on stretchable and transparent substrates made the device stretchable up to 20% with an electrical impedance increment of 26%, maintaining its high optical transparency. Also, negligible light-induced artifacts were confirmed compared with those of opaque gold electrodes, as plotted in Fig. 5b. Conventional flexible neural interfaces have difficulty to maintain intimate contact with the complex curvilinear shape of the brain surface. However, stretchable properties of the hydrogel electrode enables successful measurement of electrophysiological signals on complicated brain surface during seizure-like ictal discharge. At the same time, as the artifacts were minimized, the association between the ECoG signal and two-photon calcium imaging during ictal discharge was successfully confirmed, as shown in Fig. 5c.

Biomedical devices using hydrogels, hydrophilic polymers which have similar softness to living tissues (tens kPa), are highly conformable to complicated surfaces due to their soft nature. These properties are not only beneficial for maintaining conformal contacts, but also effective to preventing tissue damages due to Young's modulus inequality[104,122,123]. Hydrogels can have a variety of electrical, optical, and mechanical characteristics, depending on the materials being combined. Many notable studies have been conducted such as implementing anisotropic conductivity or wet surface adhesion using hydrogels[122,124–127]. Among them, conductive hydrogels with high transparency have been considered as an active material for transparent neural interface fabrication[128,129]. For example, a polyvinyl alcohol (PVA) hydrogel can achieve high transparency when PVA powder is mixed with dimethyl sulfoxide (DMSO) in specific proportions. In the synthesis of transparent PVA hydrogels, hydrogen bonding between water molecules and DMSO and the crystallinity of PVA hydrogel are strongly related[130]. Going deeper, the larger the crystalline volume, the less transparent the hydrogel as it tends to block the penetration of light. The hydrogen bonding of PVA plays the most important role in this crystalline form. If the PVA hydrogel is synthesized in pure water only, hydrogen bonds are formed between the PVA molecular chains. The remaining water molecules are then crosslinked by bonding with the -OH group of the PVA molecular chain, promoting crystalline structure growth in the z-dimension, increasing the crystalline volume. Therefore, reducing the crystalline volume is a key to form a highly transparent PVA hydrogel, and a 1:2 DMSO to water network structure fulfills this role. When the concentration of DMSO is more than 40% by weight, the oxygen atoms of DMSO bond with

hydrogen molecules of water molecules to form a 1 DMSO:2 H_2O formation, reducing the hydrogen bonding between the PVA molecular chain and water molecules. Meanwhile, PVA crystals grow two-dimensionally, with a lower volume of the PVA crystalline structure yielding high transparency. An ion-interfacing transparent neural interface, which utilizes the conformity and transparency of the PVA hydrogel, has been developed. Figure 5d shows the device schematics and highlights features of the device[129]. Unlike many other neural interfaces, which are generally implemented in plastic films, the hydrogel device minimizes disturbances of tissue fluid circulation by using a PVA hydrogel and PDMS, which have high water permeability compared to those of plastic films (e.g., polyimide)[131,132]. In addition, the electrode site and the recording site were separated using a salt bridge (KCl-saturated PVA) to implement high transparency, and light transmission, according to the wavelength band, is plotted in Fig. 5e. This transparent ion-interfacing hydrogel device successfully measured the ECoG signal of porcine brain without optical blocking. Figure 5f shows superior conformality and transparency of the device compared with conventional electrodes on the complicated cerebral cortex surface of the porcine brain.

Transparent conductive oxides (TCOs) are doped oxide compounds including metallic elements with both sufficient electrical conductivity and optical transparency[133]. The conductivity of TCOs is due to extrinsic dopants and oxygen vacancies. Without suitable doping, these oxides usually work as insulators. In general, optical band gaps of TCOs are significantly wide (>3 eV)[134,135]. TCOs show a remarkably small amount of light absorption between near-UV and near-infrared range (NIR) owing to this wide optical band gap. However, rapid transmittance level drops occur in the UV range due to strong energies of the UV light exceeding the optical band gap of TCOs. Also, optical characteristics of the NIR region is degraded mainly because of plasma edge reflections. In general, the optical transmission windows are interconnected with the conductivity of TCOs. This is because correlations exist in TCOs between carrier density and light absorption rate based on the Moss-Burstein effect[133,135]. Indium tin oxide (ITO) is the most widely used TCO for transparent thin-film fabrication. It exhibits high visible light transmittance of over 80% and sufficient electrical conductance. Although ITO has great optical and electrical properties, ITO is less likely to be considered as an active material for transparent neural interfaces due to its brittleness and poor manufacturing cost effectiveness[97,136,137]. Therefore, recent efforts to develop alternative transparent oxide-based materials to replace ITO have been made[136–143]. Due to the absence of high-performance electro-optical multimodal probes, multi-site optical stimulation with simultaneous electrical recording for microscale spatiotemporal resolution has not been well developed. In ordinary transparent neural interfaces, inevitable spatial mismatches occur between electrical recording and optogenetic stimulation points. These unavoidable differences were successfully minimized with negligible photoelectric artifacts using an ITO-coated ZnO transparent neural interface. Figure 5g shows a 4×4 micro-opto-electrode array (MOA) which transmits optical power to exact points of the electrical recording sites in waveguide format[144]. Owing to the capability of the pinpointed stimulation, a functional map of the motor cortex was verified. For example, Fig. 5h shows electrically measured firing rates from intense light stimulation of opto-electrode 9, which is colored blue in the figure. Simultaneously, both forelimbs reacted to the stimulation. In addition, it was confirmed that the size of the tissue responding to the optical stimulation varies with stimulation intensity. Figure 5i shows the stimulated region broadens as the intensity of light increases when opto-electrode 16 is manipulated.

Conductive polymers are used in various ways in implantable devices from their high mechanical flexibility that leads to reducing the risk of mechanical mismatch between the device and the soft tissues thanks to its low Young's modulus, and versatile change of electrical properties due to diversification of synthetic methods[145,146]. The excellent electrical properties of conductive polymers are attributed to the π-π conjugation molecular structure in which single and double bonds of molecules alternate[147]. Electrons belonging to this π-conjugated structures are delocalized in atoms along the π-π bond, consequently, make them free electrons. Conductive polymers have dramatically different electrical properties depending on the oxidation and reduction states of each material[148]. This is because the π-π bond exists in an oxidized state to represent a positive charge, and the dopant for neutralization of the charge coexists with the polymer in the form of an anion. Promising conductive polymers exhibiting excellent electrical conductivity have been broadly applied to implantable devices including polypyrrole (PPy)[149], polyaniline (PANI)[150], and PEDOT:PSS (poly(3,4-ethylenedioxythiophene) polystyrene sulfonate (PSS)). Among them, PEDOT:PSS represents intrinsically high optical transmittance and has the potential to have high electrical conductivity depending upon the post treatment[151]. These characteristics have been mainly used as an adhesion layer to reduce mechanical mismatch of metal-based implantable microelectrodes and to secure low electrochemical impedance[152,153]. For an example, Fig. 5j shows a schematic illustration of a transparent implantable electrode array composed of a single layer of PEDOT:PSS treated with ethylene glycol[154]. The device is highly transparent including the substrate, and this particular device for neural recording and neuromodulation by combining with optogenetics is manufactured by the simplest fabrication. Au electrode array and transparent PEDOT:PSS-EG electrode array were implanted over the right cerebral cortex of transgenic mice to figure out how much blue laser was transmitted through the electrode to the brain (Fig. 5k). As shown in Fig. 5l, the conventional Au electrode array showed significantly lower light evoked electrophysiological potentials due to low optical transmittance, whereas the PEDOT:PSS-EG electrode array accurately transmits light to the laser stimulation point. Traditionally, electro-plated PEDOT:PSS on metal electrodes or other conductive electrodes are used to reduce the impedance for neural recording[152]. However, the method of electroplating PEDOT:PSS has some complexity in the manufacturing process because the deposition of an additional conductive layer for the adhesion layer is essential. In addition, due to the intrinsic transparency of this metal layer, the deposition thickness of PEDOT:PSS is also limited to ensure the transparency of the entire electrode array. Herein, by dramatically improving the post treatment method on single layer PEDOT:PSS for enhancing its conductivity and simple lift-off process, the manufacturing cost for the transparent electrodes is significantly reduced.

TRANSPARENT IMPLANTS-FROM STRUCTURE

Although there are methods that use an intrinsically transparent material, as introduced above, to design the transparent MEAs, there is another recent research trend of modifying existing materials to have optically see-through properties through structural design. One of the significant advantages of this approach is that it maintains optical transparency while minimizing the loss of the electrical properties of each material. In the following section, recent studies into various mesh structures and metallic nano wires will be introduced as two promising candidates of the structural design.

Mesh structured neural interface

Mesh structure is one of the alternatives to design transparent metal interfaces with intrinsically non-transparent materials. The optimum performance of the mesh-structured electrode lies in balancing sheet resistance (R_S) and transparency[155]. Two factors of

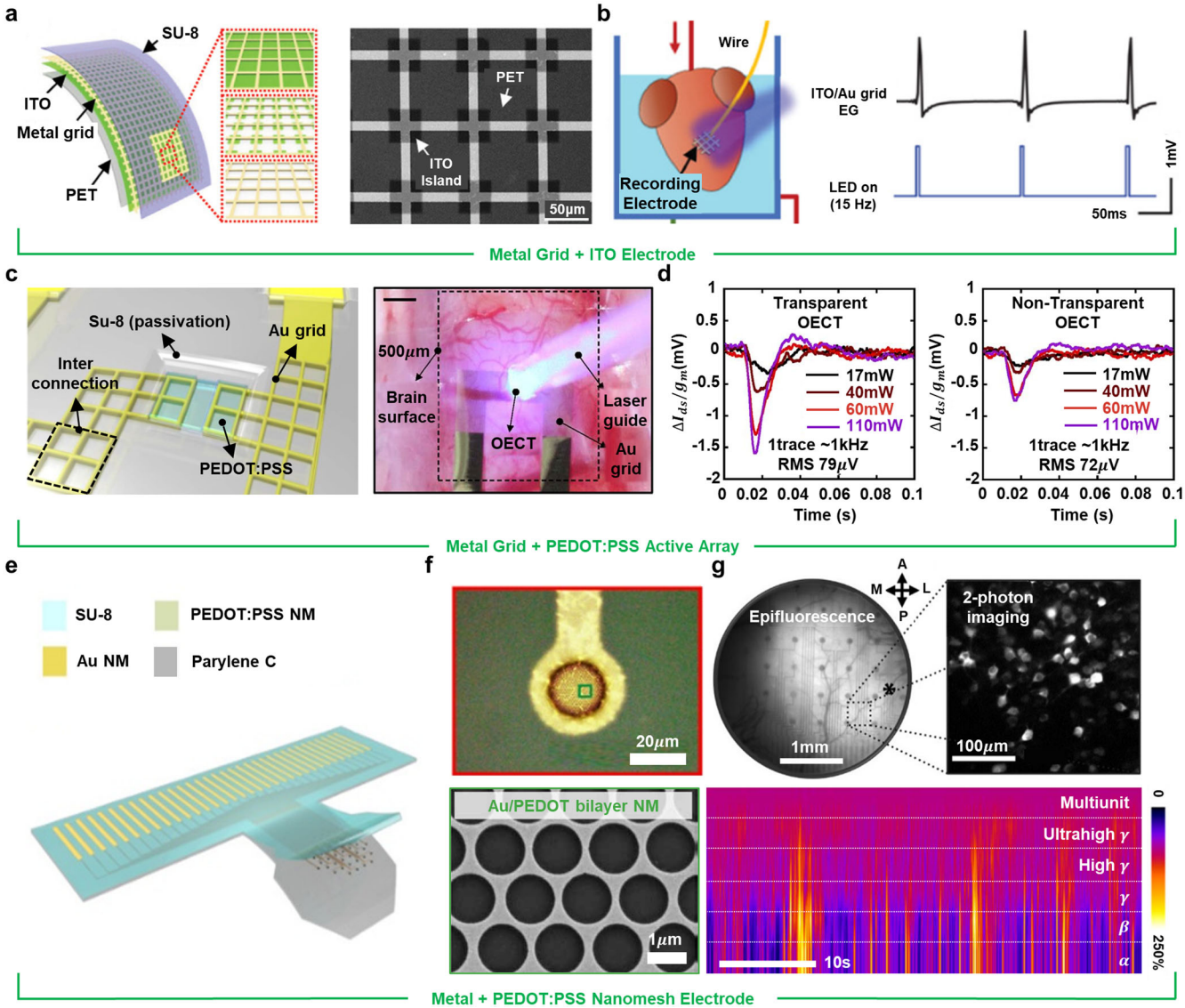

Fig. 6 Mesh structured transparent electrode arrays for multimodal sensing and stimulation of neuro-dynamics. a Transparent microelectrode arrays based on an Indium Tin oxide (ITO)/metal grid hybrid (left), metal grid on an ITO film (inset top), metal grid on an ITO island (inset middle), metal grid (inset bottom), and scanning electron microscopy (SEM) image of an ITO island with a metal grid (right). **b** Langendorff perfusion experiment setup for recording the electrophysiological signal and optogenetics simultaneously on the hearts of mice (left), and the recorded QRS complex with microelectrodes induced by blue light emitting diode (LED) (right). **c** Single cell in a transparent organic electrochemical transistors (OECTs) array (left), and conformally contacted transparent OECT on a cortical surface of a transgenic rat, stimulated with a blue laser (right). **d** In vivo evaluation conducted with transparent and non-transparent OECTs, and recorded electrocorticography (ECoG) signals evoked with blue light stimulation depending on excitation intensities. **e** Illustration of a transparent multichannel Au/PEDOT:PSS bilayer micro-electrode array (MEA). **f** Microscope image of a bilayer MEA (top), SEM image of a bilayer nanomesh MEA (bottom). **g** Simultaneous electrophysiological recording (bottom) and two-photon imaging (top right) through an epicortical bilayer MEA on the visual cortex of mice. Panels a and b reprinted with permission from ref. [162], PNAS; panels c and d reprinted with permission from ref. [167], PNAS; panels e, f, and g reprinted with permission from ref. [25], AAAS.

this structure can be modified by adjusting various mesh values (width, pitch, thickness) or the geometry of the patterns. The sheet resistance varies depending on the design of the geometrical pattern (grids, holes, pyramids, honeycombs, etc.), taking a square grid as an example, the expression for calculating Rs can be expressed as below where ρ represents specific resistance while others, h (height), w (width), and p (pitch), are mesh values. Transparency (T) can be predicted from these mesh values under the premise that the geometrical design is a grid. By substituting the mesh value with the appropriate value, the relationship between sheet resistance and transparency can be expressed by the following equation[35,156]:

$$R_{s,grid} = \frac{\rho \cdot p}{h \cdot w} = \frac{\rho}{h}\left(\frac{1-\sqrt{T}+T}{1-\sqrt{T}}\right)$$

As shown in the expression, the wider the spacing between the metal wires, the higher the transparency, along with the unavoidable high electrochemical impedance. Several studies of designing a transparent MEA using a mesh structure have used a method of coating or bonding low-impedance materials, such as conductive polymers or oxides, on a metal grid to avoid the disadvantages[157–161]. Figure 6a shows a highly transparent

conducting microelectrode array based on a metal grid (MG) hybrid with ITO[162]. Due to the low impedance and high transparency of ITO, placing the ITO in the vacant space of the MG significantly increases the charge transfer and interfacial area between the electrode and the target region without loss of transparency. The combination of ITO and the MG is possible both ways, either by adding ITO to the MG in an island form or by laying an ITO film under the MG. In the case of a hybrid microelectrode based on the ITO island type, the MG structure bridges the gaps in ITO to achieve highly flexible hybrid microelectrodes, structurally minimizing the mechanical load applied to the intrinsically brittle ITO islands. This neural microelectrode showed high transparency at 81 ± 1.9% from 400 to 800 nm with sheet resistance cut in half with 14.1 Ω sq^{-1} compared to pristine MG microelectrodes (26.8 Ω sq^{-1}). A demonstration of the electrophysiological signal was measured of the hearts of transgenic mice in vitro when stimulated with blue light LEDs (Fig. 6b). EG signals and optogenetic pacing of cardiomyocytes optically expressing channelrhodopsin-2 (ChR2) were simultaneously recorded to investigate multimodal feasibility.

To overcome the limitations of passive microelectrode array (MEA), which is poor at recording with a high resolution over a large area, an active MEA can be designed by connecting an amplifier or multiplexer to each passive electrode[163,164]. The biggest advantage of an active MEA is that it is capable of integratng electrodes with a higher scalability compared to a passive array, and a higher spatial resolution can be obtained when considering the area ratio. Examples of this are organic electrochemical transistors (OECTs), which are composed of arrays of active transistors as channels with organic components, conductive interconnects[45,165,166]. Figure 6c depicts a transparent and flexible OECT using an Au wire grid and PEDOT:PSS as active channels on a parylene substrate[167]. By optimally designing the grid width and periodicity of the 3 μm Au mesh interconnection, sufficient optical transparency and electrophysiological measurement fidelity were simultaneously obtained. To investigate the feasibility of low-light artifacts from transparent OECT, ECoG signals from transgenic mice induced by a 473 nm wavelength laser beam were recorded (Fig. 6c, right). This high transparency resulted in a reduction in the reflected light and doubled photoresponse intensity compared to the non-transparent OECT (Fig. 6d).

Another way to achieve higher spatial resolution and density is to design smaller size of a single electrode like that of single neuron[86,168]. Figure 6e shows a 32-channel Au/PEDOT:PSS bilayer MEA based on the nanomesh[25]. The most challenging part of reducing the site area to the neuron level is the difficulty of maintaining sufficiently low electrochemical impedance for recording. To resolve the challenge, a specialized bilayer structure was implemented by electroplating PEDOT:PSS on the lifted Au nano-mesh structure using a polysterene nanosphere as a mask. By virtue of a double-layer structure based on mesh, electrochemical impedance was 20 times lower than MEAs of graphene or ITO with the same site area and applicable optical transparency. Figure 6f is an optical microscope and SEM image of a single channel microelectrode, shows densely placed voids forming nano-meshes. To observe arousal changes during visual stimulation, two-photon calcium imaging of a single neuron and ECoG were recorded concurrently with the pupil diameter of awakened mice (Fig. 6g). The neuronal action potentials were classified into six level of frequency bands (α, β, γ, high γ, ultrahigh γ, and multiunit). Recorded electrophysiological activities below α band, 8–12 Hz, contains temporal information of Ca^{2+} indicator (GCaMP6s) imaging, while those of higher frequency bands contain ECoG information. This result highlights the significant benefits of multimodal functions of this work.

Metallic nanowire for neural interface

Another attractive candidate for a transparent neural interface based on metal is to use metallic nanowire (NW). The metallic NW structure has unique properties over the planar metal layer with a mesh structure such as a high effective surface area, an electrical conductivity, and an optical transparency[169,170]. Owing to these distinctive properties, the nanowire network offers an application capability for optoelectronics. Moreover, the metallic nanowire structure is suitable for interfaces with direct contacts, such as wrinkled tissues, since wire-based construction is much more mechanically flexible than those of carbon or metal oxide.

An optical image of the transparent neural interface mapping ECoG signals in 2D based on a gold nanonetwork (Au–NN) is depicted in Fig. 7a, consisting of randomly patterned Au microelectrodes with 16 channels[18]. To fabricate Au-NN, chromium, and gold layers were thermally deposited in a photoresistor layer. Next, poly (methyl methacrylate) (PMMA) nanofibers were deposited through electrospinning, serving as a hard mask for nanopatterning. After Au etching with removal of PR, the form of the microelectrodes with Au–NN is completed. One of the key challenges of designing implantable devices with metal NW is wire oxidation, causing a foreign body response that hinders long-term implantation[171,172]. Owing to the non-reactive property of Au, Au–NN microelectrodes avoid the drawback of wire oxidation. The microelectrode array exhibits 81% of transmittance and low electrochemical impedance of 33.9 kΩ at 1 kHz. In the case of metal electrodes, regardless of their geometrical structures, photoelectric artifacts induced by optical stimulation are often unavoidable. Photoelectric artifacts are proportional to the intensity of the excitation light and the amount of metal surface exposed to light. Thus, the ideal condition to minimize this issue is to limit the exposed portion of the metal surface from the light, maintaining its electrical characteristics. In nano-structured design for the electrodes, the issue of a relatively high electrochemical impedance arises because the conductive path through which electrons can move is somewhat limited compared to the film type[173]. However, the probability of electron emission by photon excitation is lowered to that extent, so it has advantageous characteristics for integration of optical modalities[174]. To investigate whether Au–NN is free from photoelectric artifacts for the practical capability of the device, simultaneous in vivo recording and light stimulation (473 nm), which excites ChR2-expressed neurons, was assessed. The device was implanted on the cortical surface of two mice groups: wild type and transgenic mice. Recorded ECoG signals during light stimulation (473 nm) on the cortical surface are presented in Fig. 7b, c. The figure exhibits the eliminated photoelectric artifact contrasted to the Au film electrode, indicating its promising feasibility for the integration of electrophysiology and optogenetics.

To overcome the challenging aspect of chronic implantation, coatings with non-reactive materials can be used[175,176]. Figure 7d shows one example: a neural interface engaging an Ag/Au core-shell nanowire (AgNW/Au)[22]. A transparent hydrogel, polyvinyl alcohol (PVA), coated the exterior of the microelectrodes for minimal loss of light, lowering electrochemical impedance, and blocking oxidation. To demonstrate its long-term durability, a reliability test was conducted in saline solution. The Ag/Au electrode with PVA remained electrochemical impedant for 5 months, while the Au-plated electrode without gel remained for 60 days. Plating thin Au on the Ag-NW established higher stretchability and more stable electrical properties compared to pristine AgNW. Ag/Au core-shell NWs performed 83% of transmittance (Fig. 7e), with low electrochemical impedance of 1.1–3.2 Ω sq^{-1}. To investigate the ability of the neural interface to monitor ECoG signals, a viral vector (AAV5-Syn-Chronos-GFP) was injected at a marmoset's motor cortex and recorded the ECoG evoked from a blue laser (473 nm) (Fig. 7f).

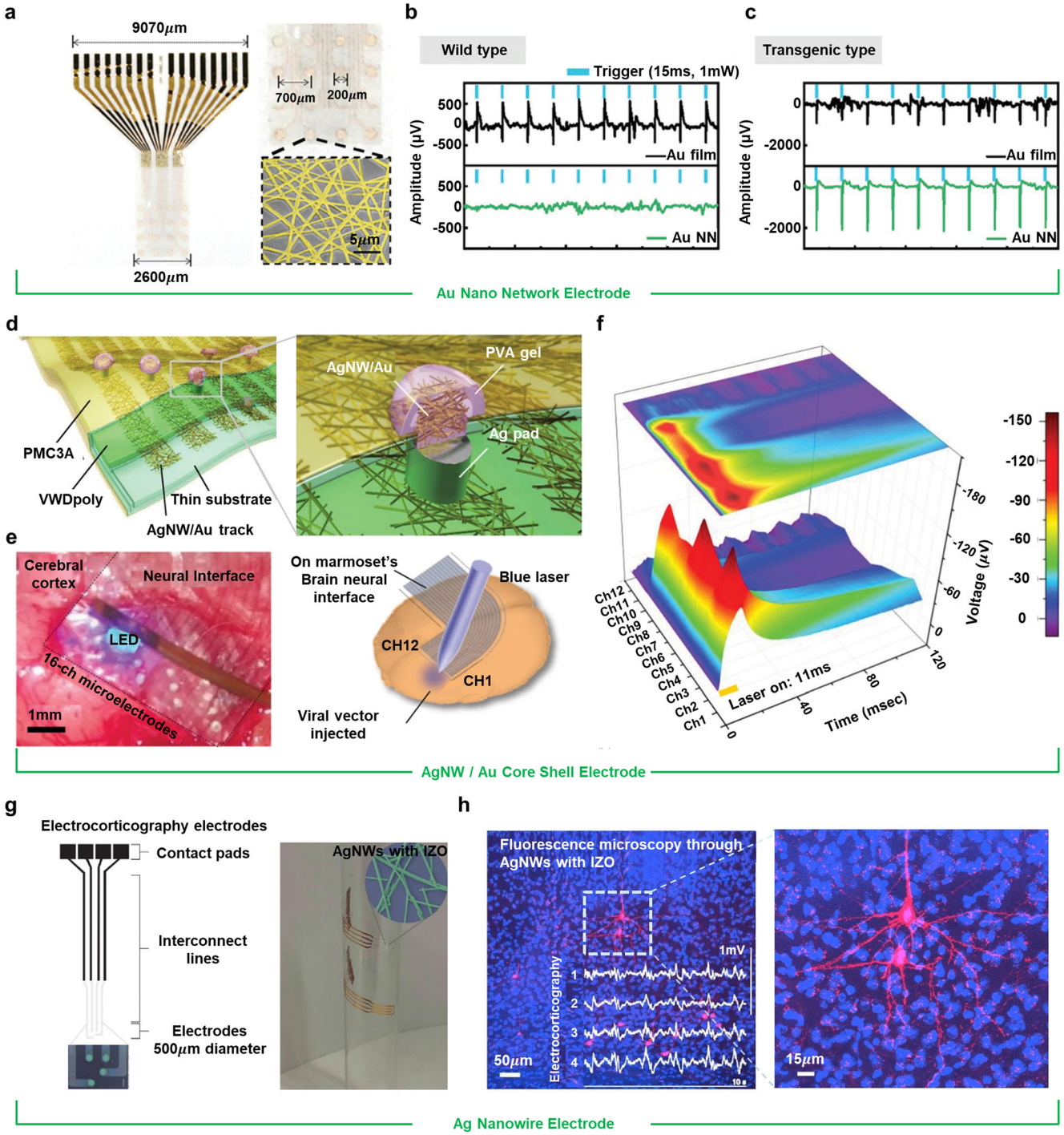

Fig. 7 Metallic nanowire-based transparent electrode arrays for multimodal sensing and stimulation of neuro-dynamics. a 16-channel Au-nano network (NN) microelectrodes array for electrocorticography (ECoG) recording. **b, c** in vivo evaluation of an artifact-free ECoG recording with gold (Au) film (opaque) and Au-NN (transparent) microelectrode arrays with optical stimulation of the cerebral cortex of wild type **b** and transgenic type (B6 Thy1-ChR2-YFP) mice **c**. **d** Schematic illustration of a multifunctional neural interface integrated with a silver (Ag)/Au core-shell nanowire (Ag nanowire (NW)/Au) with poly vinyl alcohol (PVA) gel-coated microelectrodes. **e** 16-channel AgNW/Au microelectrodes conformally contacted on cerebral cortex including light emitting diode (LED) (left), and the optogenetics in vivo setup of 12-channel AgNW/Au microelectrodes on marmoset brain (right). **f** 3D graph of the ECoG signal over time, induced by optical stimulation. **g** Schematic design of transparent ECoG electrode arrays based on AgNW with indium zinc oxide (IZO). **h** Visualization of neurons with fluorescence microscopy and ECoG recordings through AgNW/IZO microelectrodes of the cortex of mice under urethane anesthesia. Panels a, b, and c reprinted with permission from ref. [18], Wiley; panels d, e, and f reprinted with permission from ref. [22], Wiley; panels g and h reprinted with permission from ref. [179], ACS.

Transparent oxide can be an alternative candidate for defending corrosion of nanowires.[39,177,178] Fig. 7g illustrates the schematic design of the transparent electrodes with AgNW and IZO[179]. IZO not only prevents corrosion of AgNW, but also solves the problem of poor adhesion force, another drawback of AgNW. Multimodal function of optical fluorescence imaging and electrical recording from the rat cortex has been indicated without light loss or photoelectric artifacts (Fig. 7h).

OUTLOOK

To fully understand the precise mechanisms and networks of the brain, monitoring (e.g., two-photon imaging and ECoG) neural activities simultaneously with high spatial and temporal resolution and treating diseases (e.g., optical stimulation and electrical stimulation) with high selectivity are critical. To detect the signal of a specific neuron and stimulate it, the need for a multimodal device, rather than a single tool, is emphasized. Fluorescence imaging, like the two-photon imaging mentioned above, can be highly rated in terms of spatial resolution, but can be hindered by electrophysiological signals in temporal terms. The most important point of such a multimodal device is that the optical signal and the electrical signal must be accurately measured without interfering with each other and work synergistically. This review discussed the necessity of transparent neural interfaces for diagnosing and treating the brain and nervous system in three categories. First, electrophysiological approaches with optical modalities for neural implants were briefly covered, discussing recent studies that integrated two methods. Next, severe challenges from intrinsically non-transparent neural interfaces for simultaneous electrical and optical modalities were introduced, enlightening the necessity of transparent neural implantable devices. Lastly, a detailed presentation of the design of a transparent electrode array with material and structural approaches was posed. Multimodality of transparent neural interfaces can be utilized in various applications, such as the diagnosis and treatment of disorders, opening a broad pathway to next generation neuroscience and medical science.

Received: 12 January 2022; Accepted: 30 May 2022;
Published online: 29 June 2022

REFERENCES

1. Huang, S., Liu, Y., Zhao, Y., Ren, Z. & Guo, C. F. Flexible electronics: stretchable electrodes and their future. *Adv. Funct. Mater.* **29**, 1805924 (2019).
2. Shi, J. & Fang, Y. Flexible and implantable microelectrodes for chronically stable neural interfaces. *Adv. Mater.* **31**, 1804895 (2019).
3. Cho, Y., Park, S., Lee, J. & Yu, K. J. Emerging materials and technologies with applications in flexible neural implants: a comprehensive review of current issues with neural devices. *Adv. Mater.* **33**, 2005786 (2021).
4. Hong, G. & Lieber, C. M. Novel electrode technologies for neural recordings. *Nat. Rev. Neurosci.* **20**, 330–345 (2019).
5. Hejazi, M. A. et al. Hybrid diamond/carbon fiber microelectrodes enable multimodal electrical/chemical neural interfacing. *Biomaterials* **230**, 119648 (2020).
6. Kim, W. S. et al. Organ-specific, multimodal, wireless optoelectronics for high-throughput phenotyping of peripheral neural pathways. *Nat. Commun.* **12**, 1–10 (2021).
7. He, F. et al. Multimodal mapping of neural activity and cerebral blood flow reveals long-lasting neurovascular dissociations after small-scale strokes. *Sci. Adv.* **6**, eaba1933 (2020).
8. Kang, K., Cho, Y. & Yu, K. J. Novel nano-materials and nano-fabrication techniques for flexible electronic systems. *Micromachines* **9**, 263 (2018).
9. Obaid, S. N. et al. Multifunctional flexible biointerfaces for simultaneous colocalized optophysiology and electrophysiology. *Adv. Funct. Mater.* **30**, 1910027 (2020).
10. Lu, Y. et al. Ultralow impedance graphene microelectrodes with high optical transparency for simultaneous deep two-photon imaging in transgenic mice. *Adv. Funct. Mater.* **28**, 1800002 (2018).
11. Zhang, Z., Russell, L. E., Packer, A. M., Gauld, O. M. & Häusser, M. Closed-loop all-optical interrogation of neural circuits in vivo. *Nat. Methods* **15**, 1037–1040 (2018).
12. Zou, L. et al. Self-assembled multifunctional neural probes for precise integration of optogenetics and electrophysiology. *Nat. Commun.* **12**, 1–9 (2021).
13. Zhang, X., Xu, B., Pei, J. & Feng, L. Graphene and graphene-related materials as brain electrode. *J. Mater. Chem. B* **9**, 9485–9496 (2021).
14. Middya, S. et al. Microelectrode arrays for simultaneous electrophysiology and advanced optical microscopy. *Adv. Sci.* **8**, 2004434 (2021).
15. Park, D.-W. et al. Electrical neural stimulation and simultaneous in vivo monitoring with transparent graphene electrode arrays implanted in GCaMP6f mice. *ACS Nano* **12**, 148–157 (2018).
16. Park, D.-W. et al. Fabrication and utility of a transparent graphene neural electrode array for electrophysiology, in vivo imaging, and optogenetics. *Nat. Protoc.* **11**, 2201–2222 (2016).
17. Yang, W. & Yuste, R. In vivo imaging of neural activity. *Nat. Methods* **14**, 349–359 (2017).
18. Seo, J.-W. et al. Artifact-free 2D mapping of neural activity in vivo through transparent gold nanonetwork array. *Adv. Funct. Mater.* **30**, 2000896 (2020).
19. Kozai, T. D. & Vazquez, A. L. Photoelectric artefact from optogenetics and imaging on microelectrodes and bioelectronics: new challenges and opportunities. *J. Mater. Chem. B* **3**, 4965–4978 (2015).
20. Wang, L.-C. et al. The use of a double-layer platinum black-conducting polymer coating for improvement of neural recording and mitigation of photoelectric artifact. *Biosens. Bioelectron.* **145**, 111661 (2019).
21. Pisanello, F., Sileo, L. & De Vittorio, M. Micro-and nanotechnologies for optical neural interfaces. *Front. Neurosci.* **10**, 70 (2016).
22. Araki, T. et al. Long-term implantable, flexible, and transparent neural interface based on Ag/Au core–shell nanowires. *Adv. Healthc. Mater.* **8**, 1900130 (2019).
23. Araki, T. et al. Wireless monitoring using a stretchable and transparent sensor sheet containing metal nanowires. *Adv. Mater.* **32**, 1902684 (2020).
24. Kuzum, D. et al. Transparent and flexible low noise graphene electrodes for simultaneous electrophysiology and neuroimaging. *Nat. Commun.* **5**, 1–10 (2014).
25. Qiang, Y. et al. Transparent arrays of bilayer-nanomesh microelectrodes for simultaneous electrophysiology and two-photon imaging in the brain. *Sci. Adv.* **4**, eaat0626 (2018).
26. Kim, K., Park, Y. G., Hyun, B. G., Choi, M. & Park, J. U. Recent advances in transparent electronics with stretchable forms. *Adv. Mater.* **31**, 1804690 (2019).
27. Zhang, J. et al. Stretchable transparent electrode arrays for simultaneous electrical and optical interrogation of neural circuits in vivo. *Nano Lett.* **18**, 2903–2911 (2018).
28. Park, D.-W. et al. Graphene-based carbon-layered electrode array technology for neural imaging and optogenetic applications. *Nat. Commun.* **5**, 5258 (2014).
29. Kang, H., Jung, S., Jeong, S., Kim, G. & Lee, K. Polymer-metal hybrid transparent electrodes for flexible electronics. *Nat. Commun.* **6**, 1–7 (2015).
30. Hofmann, A. I., Cloutet, E. & Hadziioannou, G. Materials for transparent electrodes: from metal oxides to organic alternatives. *Adv. Electron. Mater.* **4**, 1700412 (2018).
31. Green, R. & Abidian, M. R. Conducting polymers for neural prosthetic and neural interface applications. *Adv. Mater.* **27**, 7620–7637 (2015).
32. Ye, S., Rathmell, A. R., Chen, Z., Stewart, I. E. & Wiley, B. J. Metal nanowire networks: the next generation of transparent conductors. *Adv. Mater.* **26**, 6670–6687 (2014).
33. Song, C.-H., Han, C. J., Ju, B.-K. & Kim, J.-W. Photoenhanced patterning of metal nanowire networks for fabrication of ultraflexible transparent devices. *ACS Appl. Mater. Interfaces* **8**, 480–489 (2016).
34. Jung, E. D. et al. Highly efficient flexible optoelectronic devices using metal nanowire-conducting polymer composite transparent electrode. *Electron. Mater. Lett.* **11**, 906–914 (2015).
35. Schneider, J. et al. Electrohydrodynamic nanodrip printing of high aspect ratio metal grid transparent electrodes. *Adv. Funct. Mater.* **26**, 833–840 (2016).
36. Gao, T. et al. Hierarchical graphene/metal grid structures for stable, flexible transparent conductors. *ACS Nano* **9**, 5440–5446 (2015).
37. Park, J. H. et al. Flexible and transparent metallic grid electrodes prepared by evaporative assembly. *ACS Appl. Mater. Interfaces* **6**, 12380–12387 (2014).
38. Ginting, R. T., Ovhal, M. M. & Kang, J.-W. A novel design of hybrid transparent electrodes for high performance and ultra-flexible bifunctional electrochromic-supercapacitors. *Nano Energy* **53**, 650–657 (2018).
39. Won, Y. et al. Annealing-free fabrication of highly oxidation-resistive copper nanowire composite conductors for photovoltaics. *NPG Asia Mater.* **6**, e105 (2014).
40. Park, Y., Chung, T. S., Lee, G. & Rogers, J. A. Materials chemistry of neural interface technologies and recent advances in three-dimensional systems. *Chem. Rev.* **122**, 5277–5316 (2022).

41. Wellman, S. M. et al. A materials roadmap to functional neural interface design. *Adv. Funct. Mater.* **28**, 1701269 (2018).
42. Fattahi, P., Yang, G., Kim, G. & Abidian, M. R. A review of organic and inorganic biomaterials for neural interfaces. *Adv. Mater.* **26**, 1846–1885 (2014).
43. Ferguson, M., Sharma, D., Ross, D. & Zhao, F. A critical review of microelectrode arrays and strategies for improving neural interfaces. *Adv. Healthc. Mater.* **8**, 1900558 (2019).
44. Patil, A. C. & Thakor, N. V. Implantable neurotechnologies: a review of micro-and nanoelectrodes for neural recording. *Med Biol. Eng. Comput* **54**, 23–44 (2016).
45. Lee, W. et al. Integration of organic electrochemical and field-effect transistors for ultraflexible, high temporal resolution electrophysiology arrays. *Adv. Mater.* **28**, 9722–9728 (2016).
46. Fu, T.-M. et al. Stable long-term chronic brain mapping at the single-neuron level. *Nat. Methods* **13**, 875–882 (2016).
47. He, B., Yang, L., Wilke, C. & Yuan, H. Electrophysiological imaging of brain activity and connectivity-challenges and opportunities. *IEEE Trans. Biomed. Eng.* **58**, 1918–1931 (2011).
48. Chiang, C.-H. et al. Development of a neural interface for high-definition, long-term recording in rodents and nonhuman primates. *Sci. Transl. Med.* **12**, eaay4682 (2020).
49. Jun, J. J. et al. Fully integrated silicon probes for high-density recording of neural activity. *Nature* **551**, 232–236 (2017).
50. Monai, H. et al. Calcium imaging reveals glial involvement in transcranial direct current stimulation-induced plasticity in mouse brain. *Nat. Commun.* **7**, 1–10 (2016).
51. Gu, X. et al. Long-term optical imaging of neurovascular coupling in mouse cortex using GCaMP6f and intrinsic hemodynamic signals. *NeuroImage* **165**, 251–264 (2018).
52. Rao, J., Dragulescu-Andrasi, A. & Yao, H. Fluorescence imaging in vivo: recent advances. *Curr. Opin. Biotechnol.* **18**, 17–25 (2007).
53. Barretto, R. P., Messerschmidt, B. & Schnitzer, M. J. In vivo fluorescence imaging with high-resolution microlenses. *Nat. Methods* **6**, 511–512 (2009).
54. Chemla, S. & Chavane, F. Voltage-sensitive dye imaging: technique review and models. *J. Physiol. Paris* **104**, 40–50 (2010).
55. Brown, C. E., Aminoltejari, K., Erb, H., Winship, I. R. & Murphy, T. H. In vivo voltage-sensitive dye imaging in adult mice reveals that somatosensory maps lost to stroke are replaced over weeks by new structural and functional circuits with prolonged modes of activation within both the peri-infarct zone and distant sites. *J. Neurosci.* **29**, 1719–1734 (2009).
56. Lam, S. et al. In vivo optical coherence tomography imaging of preinvasive bronchial lesions. *Clin. Cancer Res.* **14**, 2006–2011 (2008).
57. Wang, B., Lu, Y. & Yao, X. In vivo optical coherence tomography of stimulus-evoked intrinsic optical signals in mouse retinas. *J. Biomed. Opt.* **21**, 096010 (2016).
58. Hoshi, Y. & Yamada, Y. Overview of diffuse optical tomography and its clinical applications. *J. Biomed. Opt.* **21**, 091312 (2016).
59. Lee, C. W., Cooper, R. J. & Austin, T. Diffuse optical tomography to investigate the newborn brain. *Pediatr. Res.* **82**, 376–386 (2017).
60. Tang, Q. et al. In vivo voltage-sensitive dye imaging of subcortical brain function. *Sci. Rep.* **5**, 17325 (2015).
61. Tang, Q. et al. In vivo mesoscopic voltage-sensitive dye imaging of brain activation. *Sci. Rep.* **6**, 25269 (2016).
62. Civillico, E. F. & Contreras, D. Integration of evoked responses in supragranular cortex studied with optical recordings in vivo. *J. Neurophysiol.* **96**, 336–351 (2006).
63. Krasnow, A. M., Ford, M. C., Valdivia, L. E., Wilson, S. W. & Attwell, D. Regulation of developing myelin sheath elongation by oligodendrocyte calcium transients in vivo. *Nat. Neurosci.* **21**, 24–28 (2018).
64. Yang, H. H. et al. Subcellular imaging of voltage and calcium signals reveals neural processing in vivo. *Cell* **166**, 245–257 (2016).
65. Senarathna, J. et al. A miniature multi-contrast microscope for functional imaging in freely behaving animals. *Nat. Commun.* **10**, 1–13 (2019).
66. Prasad, A., Chaichi, A., Kelley, D. P., Francis, J. & Gartia, M. R. Current and future functional imaging techniques for post-traumatic stress disorder. *RSC Adv.* **9**, 24568–24594 (2019).
67. Cagnan, H., Denison, T., McIntyre, C. & Brown, P. Emerging technologies for improved deep brain stimulation. *Nat. Biotechnol.* **37**, 1024–1033 (2019).
68. Krause, M. R., Vieira, P. G., Csorba, B. A., Pilly, P. K. & Pack, C. C. Transcranial alternating current stimulation entrains single-neuron activity in the primate brain. *Proc. Natl Acad. Sci. USA* **116**, 5747–5755 (2019).
69. Chen, R. et al. Deep brain optogenetics without intracranial surgery. *Nat. Biotechnol.* **39**, 161–164 (2021).
70. Chen, S. et al. Near-infrared deep brain stimulation via upconversion nanoparticle–mediated optogenetics. *Science* **359**, 679–684 (2018).
71. Montgomery, K. L. et al. Wirelessly powered, fully internal optogenetics for brain, spinal and peripheral circuits in mice. *Nat. Methods* **12**, 969–974 (2015).
72. Lee, H. J., Choi, N., Yoon, E.-S. & Cho, I.-J. MEMS devices for drug delivery. *Adv. Drug Del. Rev.* **128**, 132–147 (2018).
73. Lee, J. et al. Flexible, sticky, and biodegradable wireless device for drug delivery to brain tumors. *Nat. Commun.* **10**, 1–9 (2019).
74. Dagdeviren, C. et al. Miniaturized neural system for chronic, local intracerebral drug delivery. *Sci. Transl. Med.* **10**, eaan2742 (2018).
75. Diana, M. et al. Rehabilitating the addicted brain with transcranial magnetic stimulation. *Nat. Rev. Neurosci.* **18**, 685–693 (2017).
76. Klein, M. M. et al. Transcranial magnetic stimulation of the brain: guidelines for pain treatment research. *Pain* **156**, 1601–1614 (2015).
77. Zhao, S. et al. Full activation pattern mapping by simultaneous deep brain stimulation and fMRI with graphene fiber electrodes. *Nat. Commun.* **11**, 1–12 (2020).
78. Opie, N. L. et al. Focal stimulation of the sheep motor cortex with a chronically implanted minimally invasive electrode array mounted on an endovascular stent. *Nat. Biomed. Eng.* **2**, 907–914 (2018).
79. Vissani, M., Isaias, I. U. & Mazzoni, A. Deep brain stimulation: a review of the open neural engineering challenges. *J. Neural Eng.* **17**, 051002 (2020).
80. Mahmoudi, P., Veladi, H. & Pakdel, F. G. Optogenetics, tools and applications in neurobiology. *J. Med. Signals Sens.* **7**, 71–79 (2017).
81. Kim, C. Y. et al. Soft subdermal implant capable of wireless battery charging and programmable controls for applications in optogenetics. *Nat. Commun.* **12**, 1–13 (2021).
82. Wang, L. et al. Ultrasoft and highly stretchable hydrogel optical fibers for in vivo optogenetic modulations. *Adv. Opt. Mater.* **6**, 1800427 (2018).
83. Shokoueinejad, M. et al. Progress in the field of micro-electrocorticography. *Micromachines* **10**, 62 (2019).
84. Alahi, M. E. E. et al. Recent advancement of electrocorticography (ECoG) electrodes for chronic neural recording/stimulation. *Mater. Today Commun.* **29**, 102853 (2021).
85. Renz, A. F. et al. Opto-E-Dura: a soft, stretchable ECoG array for multimodal, multiscale neuroscience. *Adv. Healthc. Mater.* **9**, 2000814 (2020).
86. Shin, H. et al. 3D high-density microelectrode array with optical stimulation and drug delivery for investigating neural circuit dynamics. *Nat. Commun.* **12**, 1–18 (2021).
87. Buzsáki, G. et al. Tools for probing local circuits: high-density silicon probes combined with optogenetics. *Neuron* **86**, 92–105 (2015).
88. Yazdan-Shahmorad, A., Silversmith, D. B., Kharazia, V. & Sabes, P. N. Targeted cortical reorganization using optogenetics in non-human primates. *eLife* **7**, e31034 (2018).
89. Kim, K. et al. Artifact-free and high-temporal-resolution in vivo opto-electrophysiology with microLED optoelectrodes. *Nat. Commun.* **11**, 2063 (2020).
90. Richner, T. J. et al. Optogenetic micro-electrocorticography for modulating and localizing cerebral cortex activity. *J. Neural Eng.* **11**, 016010 (2014).
91. Repina, N. A., Rosenbloom, A., Mukherjee, A., Schaffer, D. V. & Kane, R. S. At light speed: advances in optogenetic systems for regulating cell signaling and behavior. *Annu. Rev. Chem. Biomol. Eng.* **8**, 13–39 (2017).
92. Shirai, F. & Hayashi-Takagi, A. Optogenetics: applications in psychiatric research. *Psychiatry Clin. Neurosci.* **71**, 363–372 (2017).
93. Montgomery, K. L., Iyer, S. M., Christensen, A. J., Deisseroth, K. & Delp, S. L. Beyond the brain: optogenetic control in the spinal cord and peripheral nervous system. *Sci. Transl. Med.* **8**, 337rv335–337rv335 (2016).
94. Cardin, J. A. et al. Targeted optogenetic stimulation and recording of neurons in vivo using cell-type-specific expression of Channelrhodopsin-2. *Nat. Protoc.* **5**, 247–254 (2010).
95. Cho, I. H., Shin, H., Lee, H. J. & Cho, I.-J. Effects of fabrication process variation on impedance of neural probe microelectrodes. *J. Electr. Eng. Technol.* **10**, 1138–1143 (2015).
96. Jang, H. et al. Graphene-based flexible and stretchable electronics. *Adv. Mater.* **28**, 4184–4202 (2016).
97. Bi, Y. G. et al. Ultrathin metal films as the transparent electrode in ITO-free organic optoelectronic devices. *Adv. Opt. Mater.* **7**, 1800778 (2019).
98. Pang, S., Hernandez, Y., Feng, X. & Mullen, K. Graphene as transparent electrode material for organic electronics. *Adv. Mater.* **23**, 2779–2795 (2011).
99. Biswas, C. & Lee, Y. H. Graphene versus carbon nanotubes in electronic devices. *Adv. Funct. Mater.* **21**, 3806–3826 (2011).
100. Guan, S., Wang, J. & Fang, Y. Transparent graphene bioelectronics as a new tool for multimodal neural interfaces. *Nano Today* **26**, 13–15 (2019).
101. Gomez-Navarro, C. et al. Atomic structure of reduced graphene oxide. *Nano Lett.* **10**, 1144–1148 (2010).
102. Lee, C., Wei, X., Kysar, J. W. & Hone, J. Measurement of the elastic properties and intrinsic strength of monolayer graphene. *Science* **321**, 385–388 (2008).
103. Nair, R. R. et al. Fine structure constant defines visual transparency of graphene. *Science* **320**, 1308–1308 (2008).

104. McCoul, D., Hu, W., Gao, M., Mehta, V. & Pei, Q. Recent advances in stretchable and transparent electronic materials. *Adv. Electron. Mater.* **2**, 1500407 (2016).
105. Lee, M. et al. Graphene-electrode array for brain map remodeling of the cortical surface. *NPG Asia Mater.* **13**, 65 (2021).
106. Kim, K. S. et al. Large-scale pattern growth of graphene films for stretchable transparent electrodes. *Nature* **457**, 706–710 (2009).
107. Yang, L. et al. Highly crumpled all-carbon transistors for brain activity recording. *Nano Lett.* **17**, 71–77 (2017).
108. Chen, T., Xue, Y., Roy, A. K. & Dai, L. Transparent and stretchable high-performance supercapacitors based on wrinkled graphene electrodes. *ACS Nano* **8**, 1039–1046 (2014).
109. Thunemann, M. et al. Deep 2-photon imaging and artifact-free optogenetics through transparent graphene microelectrode arrays. *Nat. Commun.* **9**, 2035 (2018).
110. Wang, M. et al. Flexible neural probes with optical artifact-suppressing modification and biofriendly polypeptide coating. *Micromachines* **13**, 199 (2022).
111. Niu, C. Carbon nanotube transparent conducting films. *MRS Bull.* **36**, 766–773 (2011).
112. Schnorr, J. M. & Swager, T. M. Emerging applications of carbon nanotubes. *Chem. Mater.* **23**, 646–657 (2010).
113. Lau, A. K.-T. & Hui, D. The revolutionary creation of new advanced materials—carbon nanotube composites. *Compos. B. Eng.* **33**, 263–277 (2002).
114. Baughman, R. H., Zakhidov, A. A. & De Heer, W. A. Carbon nanotubes–the route toward applications. *Science* **297**, 787–792 (2002).
115. Li, Z. et al. Large area, highly transparent carbon nanotube spiderwebs for energy harvesting. *J. Mater. Chem.* **20**, 7236–7240 (2010).
116. Fanchini, G., Miller, S., Parekh, B. B. & Chhowalla, M. Optical anisotropy in single-walled carbon nanotube thin films: implications for transparent and conducting electrodes in organic photovoltaics. *Nano Lett.* **8**, 2176–2179 (2008).
117. Murakami, Y., Einarsson, E., Edamura, T. & Maruyama, S. Polarization dependence of the optical absorption of single-walled carbon nanotubes. *Phys. Rev. Lett.* **94**, 087402 (2005).
118. Lin, C. M., Lee, Y. T., Yeh, S. R. & Fang, W. Flexible carbon nanotubes electrode for neural recording. *Biosens. Bioelectron.* **24**, 2791–2797 (2009).
119. Hu, X. et al. Large-scale flexible and highly conductive carbon transparent electrodes via roll-to-roll process and its high performance lab-scale indium tin oxide-free polymer solar cells. *Chem. Mater.* **26**, 6293–6302 (2014).
120. Geng, H.-Z. et al. Effect of acid treatment on carbon nanotube-based flexible transparent conducting films. *J. Am. Chem. Soc.* **129**, 7758–7759 (2007).
121. Jeon, I. et al. High-performance solution-processed double-walled carbon nanotube transparent electrode for perovskite solar cells. *Adv. Energy Mater.* **9**, 1901204 (2019).
122. Ge, G. et al. Stretchable, transparent, and self-patterned hydrogel-based pressure sensor for human motions detection. *Adv. Funct. Mater.* **28**, 1802576 (2018).
123. Yang, C. & Suo, Z. Hydrogel ionotronics. *Nat. Rev. Mater.* **3**, 125–142 (2018).
124. Deng, J. et al. Electrical bioadhesive interface for bioelectronics. *Nat. Mater.* **20**, 229–236 (2021).
125. Pei, X., Zhang, H., Zhou, Y., Zhou, L. & Fu, J. Stretchable, self-healing and tissue-adhesive zwitterionic hydrogels as strain sensors for wireless monitoring of organ motions. *Mater. Horiz.* **7**, 1872–1882 (2020).
126. Zhang, J. et al. Highly stretchable and self-healable MXene/polyvinyl alcohol hydrogel electrode for wearable capacitive electronic skin. *Adv. Electron. Mater.* **5**, 1900285 (2019).
127. Sim, H. J. et al. Self-healing electrode with high electrical conductivity and mechanical strength for artificial electronic skin. *ACS Appl. Mater. Interfaces* **11**, 46026–46033 (2019).
128. Jia, M. & Rolandi, M. Soft and ion-conducting materials in bioelectronics: from conducting polymers to hydrogels. *Adv. Healthc. Mater.* **9**, e1901372 (2020).
129. Nishimura, A. et al. Totally transparent hydrogel-based subdural electrode with patterned salt bridge. *Biomed. Microdevices* **22**, 57 (2020).
130. Hou, Y. et al. Preparation of PVA hydrogel with high-transparence and investigations of its transparent mechanism. *RSC Adv.* **5**, 24023–24030 (2015).
131. Lim, C. et al. Tissue-like skin-device interface for wearable bioelectronics by using ultrasoft, mass-permeable, and low-impedance hydrogels. *Sci. Adv.* **7**, eabd3716 (2021).
132. Sasaki, M. et al. Highly conductive stretchable and biocompatible electrode-hydrogel hybrids for advanced tissue engineering. *Adv. Healthc. Mater.* **3**, 1919–1927 (2014).
133. Coutts, T. J., Young, D. L. & Li, X. Characterization of transparent conducting oxides. *MRS Bull.* **25**, 58–65 (2000).
134. Oh, S. H. et al. Low-temperature growth and electronic structures of ambipolar Yb-doped zinc tin oxide transparent thin films. *Appl. Surf. Sci.* **441**, 49–54 (2018).
135. Afre, R. A., Sharma, N., Sharon, M. & Sharon, M. Transparent conducting oxide films for various applications: a review. *Rev. Adv. Mater. Sci.* **53**, 79–89 (2018).
136. Ihn, S.-G. et al. ITO-free inverted polymer solar cells using a GZO cathode modified by ZnO. *Sol. Energy Mater. Sol. Cells* **95**, 1610–1614 (2011).
137. Sim, S. H. et al. Indium-free amorphous Ca–Al–O thin film as a transparent conducting oxide. *Chem. Mater.* **31**, 8019–8025 (2019).
138. Minami, T. New n-type transparent conducting oxides. *MRS Bull.* **25**, 38–44 (2000).
139. Sarma, B., Barman, D. & Sarma, B. K. AZO (Al:ZnO) thin films with high figure of merit as stable indium free transparent conducting oxide. *Appl. Surf. Sci.* **479**, 786–795 (2019).
140. Sarma, B. & Sarma, B. K. Role of residual stress and texture of ZnO nanocrystals on electro-optical properties of ZnO/Ag/ZnO multilayer transparent conductors. *J. Alloy. Compd.* **734**, 210–219 (2018).
141. Hu, L. et al. La2/3Sr1/3VO3 thin films: a new p-type transparent conducting oxide with very high figure of merit. *Adv. Electron. Mater.* **4**, 1700476 (2018).
142. Kim, B. H. et al. High mobility in nanocrystal-based transparent conducting oxide thin films. *ACS Nano* **12**, 3200–3208 (2018).
143. Jiang, F.-X., Tong, R.-X., Yan, Z., Ji, L.-F. & Xu, X.-H. d-electron-dependent transparent conducting oxide of V-doped ZnO thin films. *J. Alloy. Compd.* **822**, 153706 (2020).
144. Lee, J., Ozden, I., Song, Y. K. & Nurmikko, A. V. Transparent intracortical microprobe array for simultaneous spatiotemporal optical stimulation and multichannel electrical recording. *Nat. Methods* **12**, 1157–1162 (2015).
145. Zhan, C. et al. Conductive polymer nanocomposites: a critical review of modern advanced devices. *J. Mater. Chem. C.* **5**, 1569–1585 (2017).
146. Bettucci, O., Matrone, G. M. & Santoro, F. Conductive polymer-based bioelectronic platforms toward sustainable and biointegrated devices: a journey from skin to brain across human body interfaces. *Adv. Mater. Technol.* **7**, 2100293 (2021).
147. Wang, Y. et al. A highly stretchable, transparent, and conductive polymer. *Sci. Adv.* **3**, e1602076 (2017).
148. Chen, J. et al. An overview of stretchable strain sensors from conductive polymer nanocomposites. *J. Mater. Chem. C.* **7**, 11710–11730 (2019).
149. Han, L. et al. Transparent, adhesive, and conductive hydrogel for soft bioelectronics based on light-transmitting polydopamine-doped polypyrrole nanofibrils. *Chem. Mater.* **30**, 5561–5572 (2018).
150. Das, S., Dutta, K. & Kundu, P. P. Nickel nanocatalysts supported on sulfonated polyaniline: potential toward methanol oxidation and as anode materials for DMFCs. *J. Mater. Chem. A* **3**, 11349–11357 (2015).
151. Kayser, L. V. & Lipomi, D. J. Stretchable conductive polymers and composites based on PEDOT and PEDOT: PSS. *Adv. Mater.* **31**, 1806133 (2019).
152. Kshirsagar, P. et al. Transparent graphene/PEDOT:PSS microelectrodes for electro- and optophysiology. *Adv. Mater. Technol.* **4**, 1800318 (2019).
153. Carli, S. et al. Electrodeposited PEDOT: Nafion composite for neural recording and stimulation. *Adv. Healthc. Mater.* **8**, 1900765 (2019).
154. Cho, Y. U. et al. Ultra-low cost, facile fabrication of transparent neural electrode array for electrocorticography with photoelectric artifact-free optogenetics. *Adv. Funct. Mater.* **32**, 2105568 (2021).
155. Jin, Y. et al. Site-selective growth of patterned silver grid networks as flexible transparent conductive film by using poly(dopamine) at room temperature. *ACS Appl. Mater. Interfaces* **6**, 1447–1453 (2014).
156. Jung, S. et al. Extremely flexible transparent conducting electrodes for organic devices. *Adv. Energy Mater.* **4**, 1300474 (2014).
157. Seo, K. J. et al. Transparent, flexible, penetrating microelectrode arrays with capabilities of single-unit electrophysiology. *Adv. Biosyst.* **3**, e1800276 (2019).
158. Kim, Y. H., Müller-Meskamp, L. & Leo, K. Ultratransparent polymer/semi-transparent silver grid hybrid electrodes for small-molecule organic solar cells. *Adv. Energy Mater.* **5**, 1401822 (2015).
159. Zhou, W. et al. Copper mesh templated by breath-figure polymer films as flexible transparent electrodes for organic photovoltaic devices. *ACS Appl. Mater. Interfaces* **8**, 11122–11127 (2016).
160. Qiang, Y. et al. Bilayer nanomesh structures for transparent recording and stimulating microelectrodes. *Adv. Funct. Mater.* **27**, 1704117 (2017).
161. Seo, K. J. et al. Transparent electrophysiology microelectrodes and interconnects from metal nanomesh. *ACS Nano* **11**, 4365–4372 (2017).
162. Chen, Z. et al. Flexible and transparent metal oxide/metal grid hybrid interfaces for electrophysiology and optogenetics. *Adv. Mater. Technol.* **5**, 2000322 (2020).
163. Fang, H. et al. Capacitively coupled arrays of multiplexed flexible silicon transistors for long-term cardiac electrophysiology. *Nat. Biomed. Eng.* **1**, 0038 (2017).
164. Kim, D.-H. et al. Epidermal electronics. *Science* **333**, 838–843 (2011).
165. Khodagholy, D. et al. In vivo recordings of brain activity using organic transistors. *Nat. Commun.* **4**, 1575 (2013).
166. Khodagholy, D. et al. High transconductance organic electrochemical transistors. *Nat. Commun.* **4**, 2133 (2013).
167. Lee, W. et al. Transparent, conformable, active multielectrode array using organic electrochemical transistors. *Proc. Natl Acad. Sci. USA* **114**, 10554–10559 (2017).
168. Tsai, D., Sawyer, D., Bradd, A., Yuste, R. & Shepard, K. L. A very large-scale microelectrode array for cellular-resolution electrophysiology. *Nat. Commun.* **8**, 1802 (2017).

169. Song, M. et al. Highly efficient and bendable organic solar cells with solution-processed silver nanowire electrodes. *Adv. Funct. Mater.* **23**, 4177–4184 (2013).
170. Kang, S. et al. Capillary printing of highly aligned silver nanowire transparent electrodes for high-performance optoelectronic devices. *Nano Lett.* **15**, 7933–7942 (2015).
171. Ahn, Y., Jeong, Y. & Lee, Y. Improved thermal oxidation stability of solution-processable silver nanowire transparent electrode by reduced graphene oxide. *ACS Appl. Mater. Interfaces* **4**, 6410–6414 (2012).
172. Alotaibi, F., Tung, T. T., Nine, M. J., Coghlan, C. J. & Losic, D. Silver nanowires with pristine graphene oxidation barriers for stable and high performance transparent conductive films. *ACS Appl. Nano Mater.* **1**, 2249–2260 (2018).
173. Hsu, P. C. et al. Performance enhancement of metal nanowire transparent conducting electrodes by mesoscale metal wires. *Nat. Commun.* **4**, 2522 (2013).
174. Yoo, J. et al. Long-term intracellular recording of optogenetically-induced electrical activities using vertical nanowire multi electrode array. *Sci. Rep.* **10**, 4279 (2020).
175. Choi, S. et al. Highly conductive, stretchable and biocompatible Ag–Au core–sheath nanowire composite for wearable and implantable bioelectronics. *Nat. Nanotechnol.* **13**, 1048–1056 (2018).
176. Kim, T. et al. Highly transparent Au-coated Ag nanowire transparent electrode with reduction in haze. *ACS Appl. Mater. Interfaces* **6**, 13527–13534 (2014).
177. Chae, W. H., Sannicolo, T. & Grossman, J. C. Double-sided graphene oxide encapsulated silver nanowire transparent electrode with improved chemical and electrical stability. *ACS Appl. Mater. Interfaces* **12**, 17909–17920 (2020).
178. Song, M. et al. Highly flexible and transparent conducting silver nanowire/ZnO composite film for organic solar cells. *Nano Res.* **7**, 1370–1379 (2014).
179. Neto, J. P. et al. Transparent and flexible electrocorticography electrode arrays based on silver nanowire networks for neural recordings. *ACS Appl. Nano Mater.* **4**, 5737–5747 (2021).

ACKNOWLEDGEMENTS

This work acknowledges the support received from the National Research Foundation of Korea (Grant nos.: NRF-2019R1A2C2086085, NRF-2021R1A4A1031437, NRF-2018M3A7B4071109).

AUTHOR CONTRIBUTIONS

Y.U.C., S.L.L., and J.-H.H. contributed equally to this work. All authors discussed the contents and commented on the manuscript.

COMPETING INTERESTS

The authors declare no competing interests.

ADDITIONAL INFORMATION

Correspondence and requests for materials should be addressed to Ki Jun Yu.

Reprints and permission information is available at http://www.nature.com/reprints

Publisher's note Springer Nature remains neutral with regard to jurisdictional claims in published maps and institutional affiliations.